

See discussions, stats, and author profiles for this publication at: <https://www.researchgate.net/publication/277952525>

Effect of Mo-Incorporation in the TiO₂ Lattice: A Mechanistic Basis for Photocatalytic Dye Degradation

ARTICLE *in* THE JOURNAL OF PHYSICAL CHEMISTRY C · JUNE 2014

Impact Factor: 4.77

READS

14

6 AUTHORS, INCLUDING:



Kaustava Bhattacharyya
Bhabha Atomic Research Centre
32 PUBLICATIONS 330 CITATIONS

[SEE PROFILE](#)



Jerina Majeed
Bhabha Atomic Research Centre
15 PUBLICATIONS 41 CITATIONS

[SEE PROFILE](#)



Krishna Dey
The Ohio State University
15 PUBLICATIONS 83 CITATIONS

[SEE PROFILE](#)



Pushan Ayyub
Tata Institute of Fundamental Research
149 PUBLICATIONS 2,993 CITATIONS

[SEE PROFILE](#)

Effect of Mo-Incorporation in the TiO₂ Lattice: A Mechanistic Basis for Photocatalytic Dye Degradation

Kaustava Bhattacharyya,^{*,†} Jerina Majed,[†] Krishna Kishore Dey,[‡] Pushan Ayyub,[§] A. K. Tyagi,[†] and S. R. Bharadwaj[†]

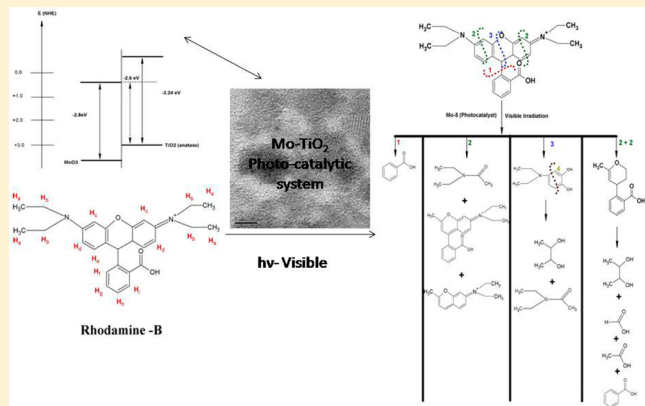
[†]Chemistry Division, Bhabha Atomic Research Centre, Mumbai 400085, India

[‡]Center of Biomedical Magnetic Resonance, Lucknow 226014, India

[§]Tata Institute of Fundamental Research, Mumbai 400005, India

S Supporting Information

ABSTRACT: Photocatalytic activity of TiO₂ (anatase) is appreciably enhanced by substitutional doping of Mo in anatase lattice, in conjunction with the incorporation of nanostructured MoO₃ within the parent anatase lattice. The photocatalyst material was characterized in detail using X-ray diffraction, Raman spectroscopy, diffuse reflectance (DR-UV–Vis spectroscopy), X-ray photoelectron spectroscopy, and electron microscopy. Photocatalysis experiments were conducted using a model rhodamine-B (Rh–B) dye reaction using both UV and visible irradiation sources. The observed trends in the case of visible irradiative source can be summarized as follows: Mo-1 < Mo-2 < Mo-5 ≫ Mo-10. Attempts were made to isolate the structural factors that control photochemical behavior of these Mo–TiO₂ photocatalysts and to correlate photocatalytic activity with different structural aspects like oxidation state, band gap, surface species, etc. Mechanistic insights were acquired from ex situ ¹H NMR studies showing different intermediates and different probable routes for the Rh–B dye degradation with UV and visible radiations. The stable intermediates were formed by a direct oxidative fragmentation route, without any evidence of the initial deethylation route. The intermediates found were benzoic acid, different amines, diols, and certain acids (mostly formic and acetic acid). The adsorption of the Rh–B dye on the catalytic surface via the N-charge centers of the Rh–B was also observed.



1. INTRODUCTION

Anatase, one of the many polymorphs of the TiO₂ family, is regarded as one of the most efficient photocatalysts for the redox reactions in both the gas, solid, and liquid–solid interphases. The detoxification of organically polluted wastewater primarily involves liquid–solid interphase reactions. Since anatase TiO₂ possesses an indirect band gap of ~3.2 eV, it acts as a photocatalyst which primarily absorbs in the UV region. One of the common routes employed to shift its absorbance toward the visible range is to dope the cationic site with different transition metal ions. Doping not only affects the band gap of the material but also leads to change in the oxidation state as well as structural parameters. It induces alterations in the redox potential, which plays a primary role in the photocatalytic activity of these doped materials.^{1–3} An effective increase in lifetime of the e⁻/h⁺ may augment the rate kinetics of the photochemical reactions. The dopants assist this strategy either by quenching one of the e⁻/h⁺ pair, thus effectively increasing the lifetime of the other or by creating requisite defect sites which effectively facilitates the photochemical activity.⁴ On the other hand, dopants can lead to the

formation of surface defect sites which trigger certain adsorption/reaction centers effective in catalysis.^{5–7} Mo can assume multiple oxidation states, and the ionic radius of Mo⁶⁺ (0.62 Å) allows it to substitute for Ti⁴⁺ in TiO₂ (0.65 Å). The Mo and W usually impart stability to the anatase TiO₂ phase.⁸

Earlier reports of the Mo-doped TiO₂ system include (a) structure–activity link of anatase V, Mo, Nb, and W-TiO₂ mixed oxides for toluene photooxidation under sunlight-type excitation,⁹ (b) probable role of Mo catalyst in quenching Rh–B, excited state leading to extended degradation of the dye, through a secondary photochemical process beyond simple deethylation,¹⁰ (c) Mo⁶⁺ incorporation in the anatase structure produces a red shift in the absorption edge and lowers the interfacial charge transfer dynamics,¹¹ (d) simultaneous cationic and anionic doping in TiO₂ with Mo and N respectively,¹² (e) Mo-doped anatase prepared by thermal hydrolysis of the peroxy–titanium complex showing the presence of Mo⁵⁺/Mo⁶⁺

Received: June 3, 2014

Revised: June 26, 2014

Published: June 26, 2014

ion doping in the TiO_2 nanostructure, (f) substantial enhancement of the photocatalytic activity in the visible region for Mo concentration of about 1.38%,¹³ (g) characterization and effect of Mo^{6+} dopants on the phase transformations of TiO_2 lattice and its photo catalytic activity dependence on the dye structure.^{14–16}

We have also explored the growth of $\text{TiO}_2\text{--MoO}_3$ nano heterostructures. $\text{TiO}_2\text{--MoO}_3$ nano composite photocatalysts have been synthesized by several methods.¹⁷ The presence of a small amount of nano dispersed MoO_3 along with TiO_2 effectively lowers the band gap and also plays a role in altering the redox potential and promoting the oxidation reactions. However, the simultaneous effect of both these factors has not been studied systematically.

Rhodamine B (Rh-B) is a dye belonging to the triphenyl-methane family, containing four N-ethyl groups at either side of the xanthene ring. The long-term presence or accumulation of these dyes in wastewater discharged from these industries is detrimental to the aquatic environment.^{18,19} There has been a comprehensive investigation of the mechanism of TiO_2 photocatalyzed reactions under UV irradiation. The photocatalytic degradation mechanisms of the triphenyl methane dye pollutants follows the usual N-dealkylation mechanism, generally involving the initial step of abstraction of one or all or several alkyl groups by the hydroxyl radicals. This results in formation of corresponding aldehyde as a byproduct. Once dealkylation is complete, fragmentation of the molecule occurs, resulting in the formation of substituted benzene compounds.^{20–22} However, one does not commonly observe routes involving only fragmentation without any dealkylation. In particular, the nature of the intermediates and the reaction pathways has not yet been clarified. However, the present study reveals the nature of the initial fragmentation and almost no dealkylation is observed.

In this report, we show that the photocatalytic properties of anatase TiO_2 are enhanced by substitutional doping of Mo in the TiO_2 lattice, simultaneously with the presence of a nano dispersed MoO_3 . Attempts were made to delineate structural factors that alter the photochemical behavior of Mo– TiO_2 . The photocatalytic activity was correlated with several parameters such as the oxidation state, band gap, surface species, etc. The photocatalysis experiments were conducted using a model Rh-B dye, and a mechanistic understanding of the photocatalytic degradation of the Rh-B dye with its adsorption properties is reported. The dealkylation step is completely absent in this case and photodegradation occurs through other routes. We report the different molecular intermediates that are involved in the Rh-B photodegradation and discuss the structural attributions leading to such a mechanism.

2. EXPERIMENTAL SECTION

a. Synthesis. A simple method was employed for the preparation of the nano titania and Mo-doped titania.²³ In this modified sol–gel process, the required stoichiometric amount of molybdic acid (Aldrich, 97%) was initially dissolved in nano pure water (conductivity 18.2 $\text{M}\Omega \text{ cm}$ ionic purity and 1–5 ppb total organic carbon content) at room temperature at a neutral pH. The molybdic acid solution was maintained at 0 °C by external application of an ice-salt mixture. To the molybdic acid solution, Ti(IV) isopropoxide solution in isopropanol (IPA) was added dropwise in a controlled manner over a period of 1 h, with vigorous stirring until the formation of a uniform gel. This gel was stirred further for 1 h to ensure incorporation of

the molybdenum precursor in the titanium gel phase. The gel was kept for nucleation for 12 h in the dark, and then IPA is removed by keeping the gel in a Petri dish for 12 h. The mass was then dried in an oven at 100 °C for 4 h. The resulting solid mass was crushed and calcined at 500 °C for 4 h. The requisite amount Mo (1.0, 2.0, 5.0, and 10 atom %) was achieved by adding a stoichiometric amount of molybdic acid solution and Ti (IV) isopropoxide. Though stoichiometric amount of molybdic acid was added to have effective substitution of Mo^{6+} at the Ti^{4+} sites in TiO_2 , yet we observed (as presented later) that the product contained nano dispersed MoO_3 along with the substitutional doping of Mo in the TiO_2 crystal lattice. Henceforth, the undoped TiO_2 (anatase) and the Mo– TiO_2 , MoO_3 , would be denoted as Mo-0, Mo-1, Mo-2, Mo-5, Mo-10, and Mo-100.

b. Characterization. Crystallographic phase analysis was carried out from powder X-ray diffraction (XRD) measurements using a Philips analytical diffractometer with Ni-filtered Cu K_α radiation. The diffractograms were recorded in the 10°–80° (2θ) region. The average crystallite size of anatase and rutile phases was determined from the Scherer equation after correcting for the instrumental broadening. UV-visible measurements in the 200–900 nm regions were conducted on a two-beam spectrometer (V-670, JASCO) with a diffuse reflectance (DR) attachment consisting of an integration sphere coated with barium sulfate. BaSO_4 was used as a reference for the same. Laser Raman spectra were recorded on a LABRAM-1 spectrometer (ISA) in the backscattering geometry and at a spectral resolution of 2 cm^{-1} . Ar^+ ion laser (488 nm) was used as an excitation source. To analyze the valence state of the photocatalysts, X-ray photoelectron spectroscopy (XPS) spectra were recorded with a Thermo VG Clamp2 Analyzer spectrometer using a $\text{Mg K}\alpha$ radiation source with the energy of 1253.6 eV, at 30 mA and band-pass energy of 8 kV. As an internal reference for the absolute binding energy, the C 1s peak (284.6 eV) was used. Transmission electron microscope (TEM) data were obtained using a 120 keV and a 200 kV FEI Tecnai machine equipped with a LaB_6 filament. TEM samples were prepared by placing a drop of the ultrasonically dispersed powder (in alcohol) on a carbon-coated copper grid and drying in air. Energy dispersive X-ray (EDS) spectroscopy was used to determine the elemental composition of the samples. Zeta potential measurements were made with a Zetasizer nano series, Malvern instruments (UK), by phase analysis light scattering with applied field strength of $2.5 \times 10^3 \text{ V/m}$. The light source was a He Ne laser (632.8 nm) operating at 4.0 mW. The experiment was carried out at 25 °C, using a quartz cuvette (universal “dip” cell) with a 10 mm light path. About 0.5 mg/mL of the sample was dispersed in 1 mL of water.

c. Photocatalysis and NMR Measurements. The molybdenum-doped TiO_2 samples so obtained were evaluated as photocatalysts for the degradation of Rhodamine B (Rh-B) dye in the presence of UV light. A 100 mL batch cylindrical pyrex glass reactor (basically a glass beaker) was employed. The irradiation source was a 400 W medium pressure Hg lamp (SAIC) located inside a quartz tube, situated perpendicularly in the reactor with 170 mW/cm^2 flux. The white light source simulating the visible spectrum emits in the 350–700 nm range with a peak around 430 nm and a flux of 234 mW/cm^2 range. For each set of experiments, the reaction mixture consisted of 50 mg of catalyst powder suspended in 100 mL of the dye solution ($\sim 10^{-5} \text{ M}$). The suspension was magnetically stirred for 30 min in the dark to establish adsorption/desorption

equilibrium. The dye-catalyst suspension was irradiated under UV light and small aliquots were withdrawn at regular intervals of time (keeping the volume of reaction mixture almost constant), and UV-visible spectra were recorded. A blank consisting of only aqueous Rh-B solution (dye, without the catalyst, was also subjected to the same procedure to cancel the effect of self-degradation of the dye). The extent of reaction was monitored by measuring the decrease in absorbance values using a spectrophotometer. The effects of pH, oxidizing agent, and oxygen atmosphere were also analyzed in the case of the Mo-5 sample. To evaluate the effect of pH on the oxidizing reaction, the pH of the suspensions (dye and Mo-5) was adjusted to pH = 2 (by adding dilute HCl) or pH = 10 (by adding dilute NaOH) and subsequently irradiated under visible light and spectroscopically analyzed. The effect of the oxidizing agent was evaluated by adding 0.5 mL of H₂O₂ to a 100 mL dye suspension. Similarly, the effect of dissolved oxygen in the liquid was studied by irradiating in the presence of O₂ flow throughout the experiment. Effect of the -OH radical was tested using a small amount (~5 mL in 100 mL) of MeOH with the Rh-B solution.

To study the time evolution of the optical absorption of the irradiated reaction mixture, aliquots of ~3 mL were withdrawn at regular time intervals and kept for sedimenting the colloidal dispersion of the catalyst for 30 min. Thereafter, the material was centrifuged and wrapped in aluminum foil in order to arrest further photobleaching. The H¹ NMR experiments were carried out at 800 MHz using a Bruker Advance spectrometer. The excitation sculpting pulse sequence²⁴ (taken directly from the Bruker pulse program library) was used for effective water suppression. Other water suppression methods were not very effective due to the highly diluted nature of the samples. The carrier frequency was carefully located on the water resonance to maximize the suppression of water. A relaxation delay of 2 s was used to let the water signal completely relax. For each sample, a 20K signal averaging was used. The 90° and other pulse powers were calibrated using standard methods. Deuterium oxide (D₂O) was added to the sample for signal locking and shimming.

3. RESULT AND DISCUSSION

a. X-ray Diffraction Studies (XRD). Figure 1 shows the characteristic powder-XRD patterns of the following typical samples studied in the present investigation: bulk anatase, nano TiO₂, and the Mo-TiO₂ samples (Mo-1, Mo-2, Mo-5, Mo-10, and Mo-100). The XRD pattern corresponding to nanotitania is found to match with that of the bulk, tetragonal anatase phase (JCPDS 21–1272). It can be inferred that this process of synthesis forms TiO₂ in the anatase phase. The XRD pattern of the other end member, MoO₃, matches with orthorhombic MoO₃ (JCPDS 05-0508). The effect of the doping of Mo in the TiO₂ anatase lattice is quite interesting. The XRD pattern of 1 and 2 atom % Mo-doped samples does not show any of the characteristic MoO₃ diffraction lines and match very well with the TiO₂ anatase phase. Therefore, within the detection limit of XRD, these samples are primarily Mo-doped anatase with a distorted tetragonal crystal structure. However, with higher amount of Mo-doping (≥ 5 atom %), we observe the MoO₃ phase in the XRD pattern along with anatase. The absence of any signature of the MO_x phase (for Mo ≤ 5 atom %) in XRD is inconclusive. First, XRD is not very sensitive to even crystalline phases below 5%. Second, the MO_x phase could be present in a noncrystalline or poorly crystalline form. Also, this

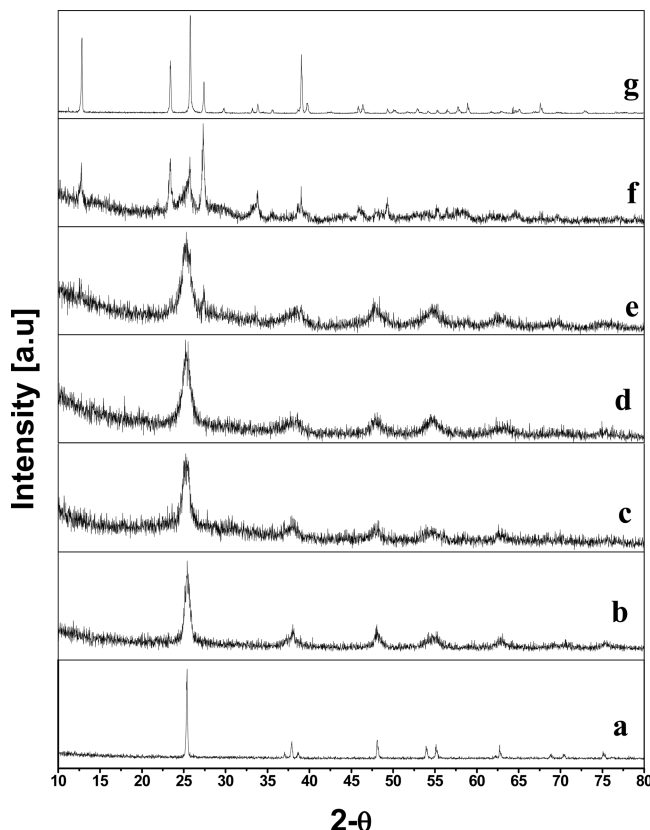


Figure 1. X-ray diffraction pattern of the Mo-TiO₂ and TiO₂ materials (a) TiO₂-anatase-bulk, (b) TiO₂-nano (anatase), (c) Mo-1, (d) Mo-2, (e) Mo-5, (f) Mo-10, and (g) Mo-100 (MoO₃).

minority phase may be in nanostructured form and any size-induced broadening will make the XRD lines more difficult to observe. For a higher percentage of MoO_x phase, it becomes easily detectable and possibly more crystalline. A better understanding of the microstructure can be obtained from spectroscopic data that are presented in the subsequent section. Consequently, it can be visualized, as the overall symmetry pattern of this doped heterostructure will not be reduced from the tetragonal symmetry; however, the crystal lattice will face a certain amount of strain. We predict it qualitatively and this is not quantified here. The XRD results further show that with a higher percentage of Mo in the TiO₂ lattice, MoO₃ exists as a nano hetero structure. However, we do not observe any shift in the (101) line of anatase TiO₂. This is expected as the ionic radius of dopant (Mo⁶⁺) is almost comparable to that of host Ti⁴⁺. However, from the EDS studies (discussed in Electron Microscopy Studies (TEM)) done later on, we unambiguously find the presence of Mo. This observation can be explained either by the presence of a small amount of Mo⁶⁺ doped in the TiO₂ lattice or by the presence of MoO₃ only as a nanoheterostructure. In either case, the presence of an amorphous, surface MoO_x phase cannot be ruled out. Compared to the parent TiO₂ phase, the XRD peaks of all synthesized samples, nano titania and Mo-titania, exhibit significant line broadening indicating the presence of smaller particle sizes. The coherently diffracting domain sizes are calculated using the Scherer equation from the broadening of the fwhm of the (101) peak, as represented in Table 1. The crystallite size of the different Mo-TiO₂ nanocomposites are as

Table 1 Coherently Diffracting Domain Sizes

sample	zeta potential value (at near neutral pH 6–7) ^a	zeta potential value after (adding Rh–B) ^b	crystallite size from XRD (nm) ^c	calculated band gap values (eV) ^d	$t_{1/2}$ values for the photodegradation of Rh–B via visible source (min) ^e
Mo-0	-22.1	-18.9	25	3.30	66
Mo-1	-25.2	-31.03	30	2.87	26
Mo-2	-30.6	-33.6	34	2.76	13
Mo-5	-34.0	-38.4	32	2.71	9
Mo-10	-38.0	-30.6	48	2.65	90

^aZeta potential values at ~neutral pH (6–7). ^bZeta potential values with Rh–B. ^cCrystallite size using Scherer equation. ^dBand gap values using the Kubelka–Munk plot. ^e $t_{1/2}$ Values for the visible irradiation reaction with the different photocatalysts.

follows: (Mo-1), 30 nm; (Mo-2), 34 nm; (Mo-5), 32 nm; and (Mo-10), 48 nm.

b. Raman Spectroscopic Studies. Figure 2 shows the Raman spectra of the bulk anatase, the Mo–TiO₂ samples

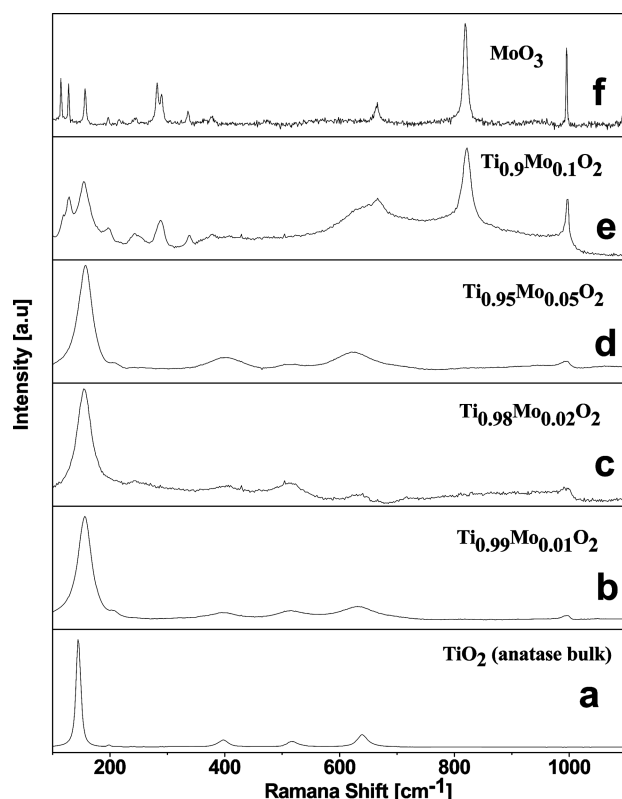


Figure 2. Raman scattering spectra of the Mo–TiO₂ and TiO₂ materials (a) TiO₂-anatase-bulk, (b) Mo-1, (c) Mo-2, (d) Mo-5, (e) Mo-10, and (f) Mo-100.

(Mo-1, Mo-2, Mo-5, and Mo-10), and MoO₃. Orthorhombic MoO₃ belongs to the D_{2h}^{16} (Pbnm) space group.^{25,26} Factor group analysis of the D_{2h}^{16} group yields 45 distinct vibrational modes out of which 24 are Raman active. The Raman spectrum of MoO₃ is shown in Figure 2f. The mode frequencies (in cm⁻¹) along with their irreducible representations are as follows 995 (A_g , B_{1g}), 819 (A_g , B_{1g}), 665 (B_{2g} , B_{3g}), 380 (B_{1g}), 336 (B_{1g} , A_g), 289 (B_{1g}), 281 (B_{2g}), 243 (B_{3g}), 215 (A_g), 198 (B_{2g}), 156 (A_g , B_{1g}), 127 (B_{2g}), 114 (B_{1g}), 96 (A_g), and 81 (A_g). The bands are at 474 (A_g , B_{1g}), 365 (A_g), and 338 (B_{1g}).

Figure 2a represents the Raman spectrum of anatase-TiO₂, which has a tetragonal unit cell and belongs to the space group D_{4h}^{19} (I41/amd).^{27,28} In accordance with the factor group analysis, there are 15 different vibrational modes out of which

there are 6 Raman active modes. The Raman band frequencies (in cm⁻¹) of TiO₂ anatase bulk as observed in Figure 2a and their respective irreducible representations are as follows: 144 (E_g), 198 (E_g), 397 (B_{1g}), 515 (A_{1g}), 520 (B_{1g}), and 640 (E_g). The Raman spectra of Mo-doped TiO₂/heterostructures samples of Figure 2 (panels b–e) shows peaks from both anatase and MoO₃ phases with a substantial shift in the intermediate regions. The Mo-1 sample (Figure 2b) shows Raman modes at 156, 205, 404, 512, 634, and 995 cm⁻¹, as compared to the bulk anatase TiO₂ peaks found at 144, 198, and 397 cm⁻¹. The full-width at half-maximum (fwhm) increases when the crystallite size decreases or the structure becomes disordered.^{29–31} It is generally seen that the Raman bands show peak shift to higher frequencies if the lattice is under some stress.^{29–31} There is a definite change in the fwhm values of bulk anatase compared to that of the Mo-doped samples. It changes from 8.79 to 26.18 cm⁻¹ (for the 144 cm⁻¹ peak). However, the peaks at 515 and 634 cm⁻¹ are almost in the same position as that of TiO₂ anatase bulk, though there is a definite increment in their fwhm values. Therefore, the shift of the peak from 144 to 156 cm⁻¹ is a representative of the lattice strain. It substantiates with our XRD information also. We are stating this qualitatively and have not tried to quantify it with the lattice parameter deduction using Reitveld or other means.

An additional band at 995 cm⁻¹ is also obtained, which is representative of the MoO₃ phase. The Raman spectra in Figure 2 (panels c and d), representing the Mo-2 and Mo-5 samples, exhibit a similar trend, with the 995 cm⁻¹ increasing in intensity. The other Raman peaks at 156, 208, 515, and 624 cm⁻¹ indicate the presence of the TiO₂ anatase phase. The presence of a peak at 995 cm⁻¹ usually shows the presence of small surface aggregates of MoO₃. This is manifested through the Mo=O (995 cm⁻¹) bond and Mo–O–Mo (broad contribution 700–940 cm⁻¹), as shown in the earlier literature.³² This signifies that for each Mo–TiO₂ sample, starting from Mo-1, there is a distinct phase separation of the MoO₃ surface phase.³² This part is quite evident, that in these samples, the MoO₃ is not in the bulk phase that we observe later in the Mo-10. The fwhm for the Mo-2 and Mo-5 samples (peak at 156 cm⁻¹) are 25.5 and 25.6 cm⁻¹, respectively. The Mo-10 sample (Figure 2e) has almost all the peaks representative of the MoO₃ bulk phase along with those for anatase. Thus, the Raman studies substantiate that the Mo–TiO₂ samples have a composite nature. This is true even for Mo-1 and Mo-2, as also suggested by the XRD data. Further, the MoO₃ phase is nano dispersed in the TiO₂ matrix. This reveals the fact that along with Mo–TiO₂, there is an amount of the MoO₃ as nano composite hetero structures. However, it is quite clear from the Raman data that in Mo-10 along with the surface phase of MoO₃, there is also definite evidence for the

bulk MoO_x. MoO₃ is probably present as a surface phase in Mo-1 to Mo-5.

c. UV–Vis –Spectroscopy (DRS- studies). The diffuse reflectance spectra (DRS) of bulk anatase (TiO₂), nano anatase (TiO₂), the Mo–TiO₂ samples (Mo-1, Mo-2, Mo-5, and Mo-10) and MoO₃ are shown in Figure 3A. Curves a and b

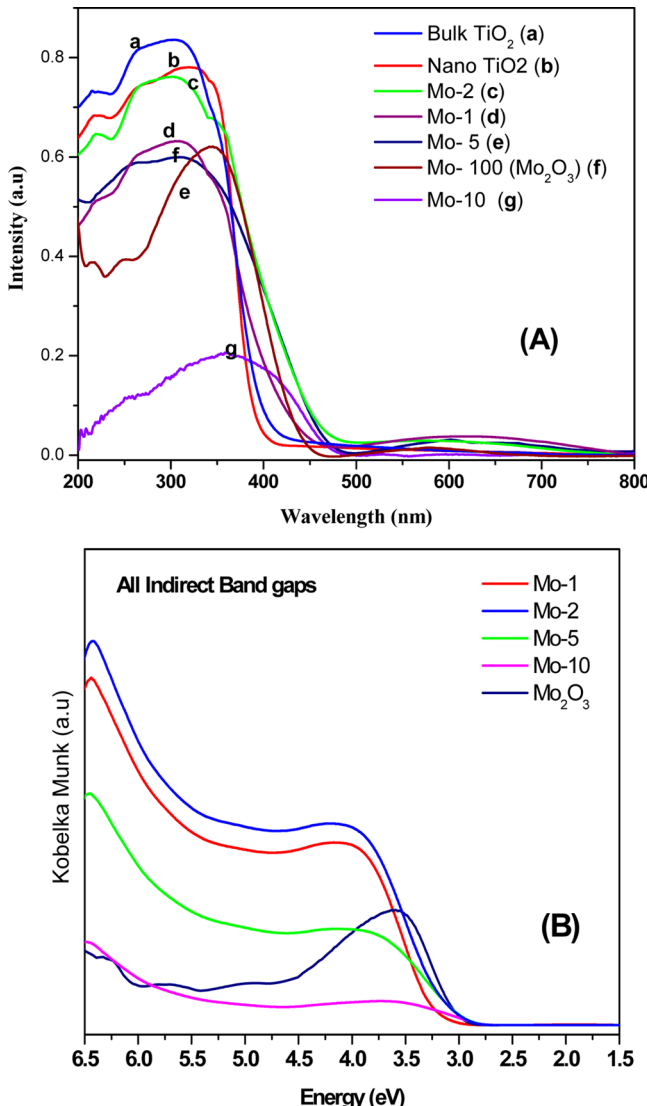


Figure 3. (A) UV–visible spectra of the Mo–TiO₂ and TiO₂ materials (a) TiO₂-anatase-bulk, (b) TiO₂-nano (anatase), (c) Mo-2, (d) Mo-1, (e) Mo-5, (f) Mo-100, and (g) Mo-10. (B) Kubelka–Munk plots of Mo–TiO₂ materials (a) Mo-1, (b) Mo-2, (c) Mo-5, (d) Mo-10, and (e) Mo-100.

represent, respectively, the spectra of bulk anatase titania and nanotitania prepared in the present investigation. There is a distinct blue shift of ~ 13 nm in the synthesized nano titania as compared to the bulk titania, which can be attributed to quantum confinement effects.^{33–35} The absorption edge for MoO₃ is generally seen at 400 nm. The intrinsic strong absorption below 400 nm in MoO₃ is due to interband (VB to CB) and excitonic transitions.³⁶ A very broad asymmetric absorption band also appears with λ_{max} between 780 and 900 nm in MoO₃ as well as in the other mixed-phase samples. This asymmetric band probably arises from a superposition of many

discrete bands,^{36–38} which is consistent with the presence of localized centers.

An estimate of the optical band gap energy (E-gap) was obtained from a plot of the Kubelka–Munk function F(R) as given below.³⁹

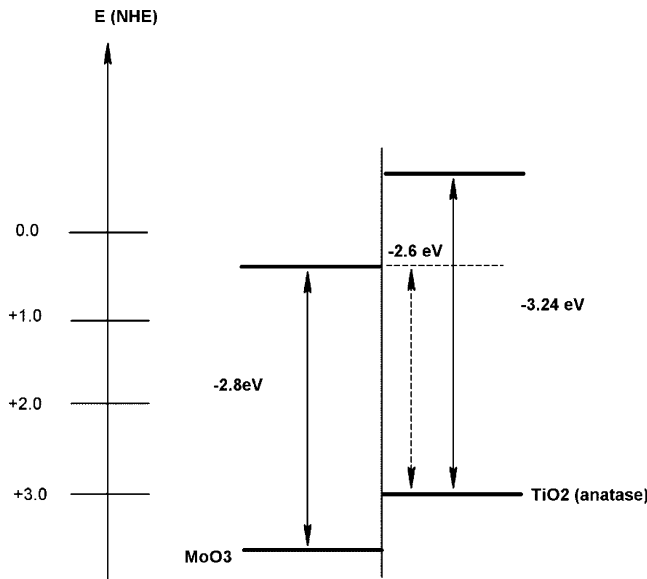
$$F(R) = A(h\nu - E_g)^{m/2} \quad (1)$$

Where $h\nu$ = photon energy and m is a constant that depends on the nature of optical transition. For a direct transition, m is 1 (if allowed) or 3 (if forbidden), while for indirect transitions, m is 4 (if allowed) or 6 (if forbidden). For a weakly absorbing semiconductor, $F(R)$ is proportional to the absorbance, A . Hence, the energy intercept of a plot of A^2 (for direct allowed transition) and $A^{1/2}$ (for indirect allowed transition) versus $h\nu$ yields the corresponding optical band gap, E_g , when the linear region is extrapolated to the zero ordinate. The Kubelka–Munk plots of these materials are depicted in Figure 3B. Consistent with the earlier results, MoO₃, TiO₂ (anatase), and Mo–TiO₂ systems possess an indirect band gap.⁴⁰ In the present set of samples, the calculated band gap from Kubelka–Munk plots range from 3.24–2.65 eV. Bulk anatase TiO₂ has a band gap of 3.24 eV, and nano TiO₂ shows a value of 3.30 eV. The Mo-100 has a band gap 2.78 eV. In the case of the Mo–TiO₂ system, there is a definite red shift in the band edges and the band gap lowers as a function of the Mo-content: E_g = 2.87 eV for Mo-1, 2.76 eV for Mo-2, and decreases consistently in Mo-5 (2.71 eV) and Mo-10 (2.65 eV), as shown in Table 1.

Theoretical calculations of the total density of states (DOS) indicate that the valence band (VB) in MoO₃ is composed of hybridized O 2p and Mo 4d states. However, the dominant contribution to the occupied region comes from the O 2p band. The contribution from Mo 4d is quite uniformly distributed in the occupied region. The lowest unoccupied energy levels of Mo have d_{xy} , d_{yz} , and d_{xz} character. The remaining d orbitals being strongly hybridized with the p_y and p_z components possess higher energy in the C B.⁴¹ The total and DOS for anatase TiO₂ were calculated to identify the contributions from various orbitals in the VB and CB. The VB corresponds mainly to the O 2p orbitals and have a uniformly distributed contribution from Ti 3d orbitals. The CB consists mainly of Ti 3d states with a smaller contribution from the O 2p states, which show two distinct structures.⁴² Consistent with the earlier literature, molybdenum oxide species may be generally dispersed on metal oxide supports due to strong X–O–Mo (X = Ti, Zr, Al, and Si) bonding.^{43–50} There was generally a mismatch between the a , c unit cell axes of MoO₃ and the a unit cell axis of anatase.^{51,52} Therefore, it is quite reasonable to believe that MoO₃ could have been nucleated on the surface of anatase TiO₂ nanocrystals to produce a nano hetero composite along with the partial doping of Mo in the TiO₂ lattice. It may be assumed that changes in band gap properties of the Mo–TiO₂ system are basically due to charge-transfer processes at the semiconductor heterojunction formed between the MoO₃ and the anatase TiO₂. Equivalently, there could also be some small contribution from the mid band gap states resulting from Mo-dopants in the TiO₂ lattice. This can be correlated with a very low presence of particular bands states in the far-IR zone, which usually reflects the mid band gap states. However, in this present manuscript, we do not have a quantitative picture about the percentage of doped Mo in TiO₂ and the nano hetero phase of MoO₃ in/on TiO₂/Mo-doped TiO₂ bulk and surface. So we present a qualitative estimate of this environment and a

quantitative correlation of the band gap properties due to nano heterostructure and/or doping still is open question. Even a low-level Mo-dopant would lead to better redox properties of the Mo–TiO₂ photocatalyst. In the model shown below in Scheme 1, the effect of the mid band gap states are neglected, and that of nano heterostructure is only considered.

Scheme 1. Band Gap Orientation of MoO₃ and TiO₂ Nano-Composites



Scheme 1 basically represents the sum total of the band gap representation of the fully developed orthorhombic MoO₃ and anatase TiO₂ heterophases both present in the bulk form. The semiconductor-anatase heterostructure contact leads to a single Fermi edge for any pair of nanostructures built up for each characteristic TiO₂ size while in contact with surface MOx entities of limited size (below 15 nm).⁵³ However, there will be a strong polydispersity in both the surface MOx particle size and that of the bulk MOx particle size. Along with that there will be additional contribution from Mo-doped TiO₂, which provides a metal anatase interface. Therefore, what we anticipate is the presence of several electronic junctions for the same sample in the Mo-1 to Mo-5 forms. However, Mo-10 will be closer to the representation in Scheme 1. The attainment of equilibrium in the Fermi edge for a nanocomposite system is complicated by the presence of several surface defect states.⁵³ We can approximate this system as a ternary system of MoOx–TiO₂ (anatase) heterojunction with the partial Mo-doping in the system.

d. X-ray Photoelectron Studies (XPS). Figure 4 shows the core level Ti 2p spectra of MoO₃–TiO₂ nano composites along with synthesized nano titania. For the nano titania, Ti 2p_{3/2} and Ti 2p_{1/2} peaks are observed at 458.5 and 464.06 eV, respectively (Figure 4a).⁵⁴ In the MoO₃–TiO₂ nano composite samples, a progressive shift is observed toward lower binding energies as compared to that of nano titania. In the case of Mo-1, the Ti 2p_{3/2} peak appears at 458.5 eV, which is the same as in TiO₂. However, in the case of the Mo-2 sample, the Ti 2p peak is observed at a lower binding energy (458.1 eV). The other two samples, Mo-5 and Mo-10, also show the Ti 2p peaks at the same position of 458.1 eV. As compared to the Mo-1 sample, Ti 2p_{3/2} peaks for other samples (Mo-2, -5, and -10)

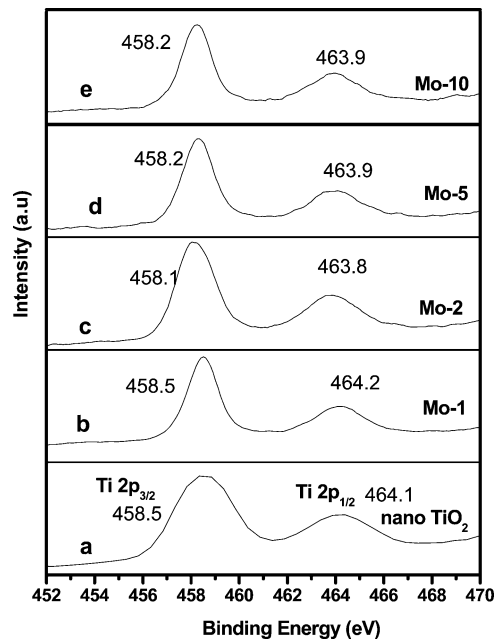


Figure 4. Ti 2p XPS spectra of Mo–TiO₂ and nano-TiO₂ samples viz. (a) nano-TiO₂; (b) Mo-1; (c) Mo-2; (d) Mo-5; and (e) Mo-10.

are broader, probably reflecting the multiple oxidation states in the Ti. The substitutional doping of a higher valent Mo⁶⁺ in the TiO₂ anatase lattice should result either in oxygen excess, or in Ti⁴⁺ vacancies, or disproportionation of the oxidation states of Ti, in order to maintain the total charge neutrality in the lattice. However, the formation of the lower valent Ti³⁺ or Ti²⁺ is not unequivocally observed in this system apart from the broadening of the Ti peak. Therefore, consistent with the earlier literature, the lowering of the binding energy suggests the formation of Ti⁴⁺ vacancies.^{55–58} Figure 5A shows the Mo 3d XPS spectrum for the different samples. The Mo-1 sample shows the Mo 3d_{5/2} at 233 eV and the 3d_{3/2} at 236.28 eV, respectively. The Mo-2 sample shows the Mo 3d_{3/2} 231.9 eV, with a negative shift of 1.1 eV. The Mo 3d_{5/2} peak comes at 235.03 eV. The Mo-5 sample shows the Mo 3d_{3/2} and Mo 3d_{5/2} peaks at 232.16 and 235.29 eV, respectively, which shows a negative shift of 0.84 eV. Mo-10 sample shows the respective XPS peaks for Mo 3d_{3/2} and Mo 3d_{5/2} at the same position of that of Mo-5 (i.e., at 232.16 and 235.29 eV). Thus, these samples also show a negative shift of 0.84 eV. Upon deconvolution (Figure 5B) of the Mo 3d_{3/2} peak, two peaks at 230.9 eV and that at 232.2 eV are found. Consistent with earlier literature, the specific peak for Mo⁵⁺ is at 231 eV and that due to Mo⁶⁺ is at 232.6 eV.⁵⁶ Upon going to the Mo peaks for the MoO₃ only, we also find the presence of the Mo⁵⁺ and Mo⁶⁺ states inherently in the MoO₃ itself (Figure 5A).⁵² The presence of Mo⁵⁺ in the Mo–TiO₂ sample therefore may be due to two reasons. One is the presence of Mo⁵⁺ (inherently) in the surface MoO₃ states that are formed. The other possibility is that of the Mo⁶⁺ being doped reduces itself partly to Mo⁵⁺ in order to maintain the charge neutrality in the lattice. In this system, it may be presumed that both these processes are simultaneously taking place. There is some amount of Mo⁵⁺ inherently in the MoO₃ states along with it that also indicates that Mo is doped partially. The later statement can be more understood in light of the O 1s and Ti⁴⁺ XPS peaks. Therefore, the above results strongly indicate that an increase in the effective Mo percentage in the system definitely leads to the

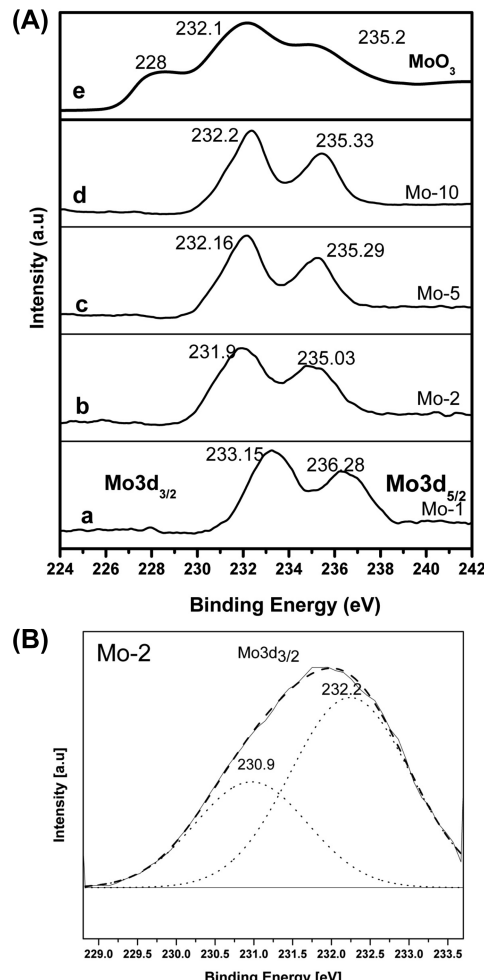


Figure 5. (A) The Mo 3d XPS spectra of the photocatalytic samples of (a) Mo-1; (b) Mo-2; (c) Mo-5; (d) Mo-10; (e) MoO_3 . (B) Deconvoluted spectra of Mo 3d_{3/2} for Mo-2 sample.

existence of the Mo^{5+} and Mo^{6+} states. The shift of the Mo peak to the lower binding energy is also a result of the presence of Mo^{5+} along with Mo^{6+} .

Another interesting observation comes from the O 1s XPS spectra of these materials. The O 1s peak for nano-TiO₂ (Figure 6) is found at 532.2 eV. The corresponding O 1s peaks for the MoO_3 sample is found at 530.8 eV, O 1s of Mo-1 and Mo-2 samples are found at 531 eV, showing a negative shift in the binding energy by ~ 1.2 eV. The Mo-5 and Mo-10 shows an O 1s XPS peak at 529.6 eV. They have further negative shift in the binding energy by ~ 2.6 eV, as compared to the O 1s of TiO₂. Deconvolution of the O 1s peak is represented in Figure 7. The O of the TiO₂ is not present under any other chemical environment except that Ti–O and –OH. Therefore, O 1s XPS spectra of nano-TiO₂ shows the presence of O corresponding to $[-\text{Ti}-\text{O}]$ (532.2 eV) and O for the surface $[-\text{OH}]$ (535 eV), which is consistent with the earlier literature (Figure 7). With the O 1s of MoO_3 sample, we get three deconvoluted peaks and the peak representing the 533.5 eV represents the O of –OH. The other two different O's at 530 and 531 eV, respectively, must be representing the O's attached to Mo with different oxidation states (Mo^{6+} and Mo^{5+}). The Mo-1 sample shows peaks at (532, 531) eV, and the Mo-2 sample yields peaks at (532, 531, and 529) eV, respectively. The intensity of the deconvoluted peak at 529 eV (Mo-2) is very low and hence

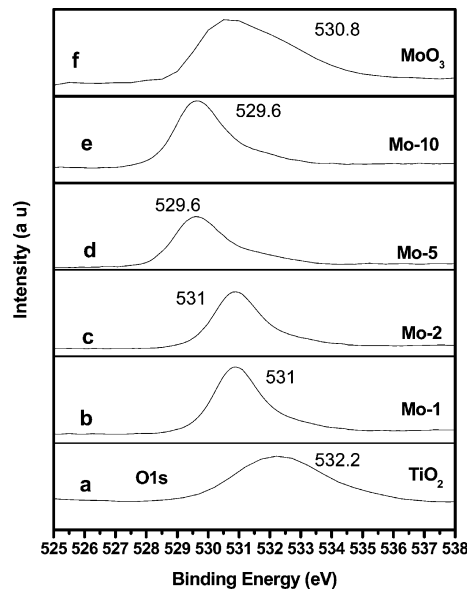


Figure 6. O 1s XPS spectra for all the photocatalytic samples (a) TiO_2 ; (b) Mo-1; (c) Mo-2; (d) Mo-5; and (e) Mo-10; (f) MoO_3 .

can be neglected. The deconvolution of the O 1s peaks of Mo-5 and Mo-10 shows two peaks at 531 and 530 eV. The Mo-2/Mo-1 sample shows representative O for the TiO₂ at 531 eV, presenting a lower binding energy as compared to that of O-(Ti–O) by 1 eV. Therefore, the O for the –OH (for Mo-2/Mo-1 sample) is also expected to be at a lower binding energy than 535 eV. This peak is found at 532 eV being consistent with the previous literature.³² Similarly for the Mo-5 and Mo-10, we get the O-(Ti–O) at 530 eV and the –O (–OH) at 531 eV. Therefore, upon deconvolution of the O peaks, we found the O present there for Ti–O and that of –O–H. However, this (deconvolution) does not hint in any of the form for the Mo-doping in the TiO₂ lattice. Nevertheless, we find that there is a systematic lowering of the bond energy (BE) of the O 1s, representing the Ti–O. Mostly this is happening due to the presence of non stoichiometry at the O site, probably due to the presence of O excess to counter the charge of Mo^{6+} doped in the TiO₂ lattice.^{59–65} Therefore, the negative shift in the O XPS peak suggests the O nonstoichiometry due to O excess. Raman studies definitely indicate the presence of MoO_3 in the Mo-doped TiO₂ lattice.

Therefore, from XPS study it can probably be inferred that there is doping in this Mo–TiO₂ system along with the presence of the nano heterostructures of MoO_3 and TiO₂. If the nano heterostructures of MoO_3 and TiO₂ only existed simultaneously, there would not be any shift that would have been present progressively in the XPS patterns of Ti and O, respectively, as we observe here. Then we could only have estimated some changes in the XPS spectra of Mo only due to the differential presence of $\text{Mo}^{6+}/\text{Mo}^{5+}$ inherently, even in the MoO_3 structure. However, we would not expect any negative shift in O 1s or in Ti 2p spectra in that scenario. The systematic difference observed in the electronic environment as reflected in their XPS spectral features definitely proves the fact that there is an electronic interaction of the $\text{Mo}^{6+}/\text{Mo}^{5+}$ with the TiO₂ lattice and that could only be understood if there is some substitutional doping of Mo in the TiO₂ anatase lattice. The XPS studies show that there is a negative shift in the binding energy of the XPS peaks for Ti, Mo, and O due to the presence

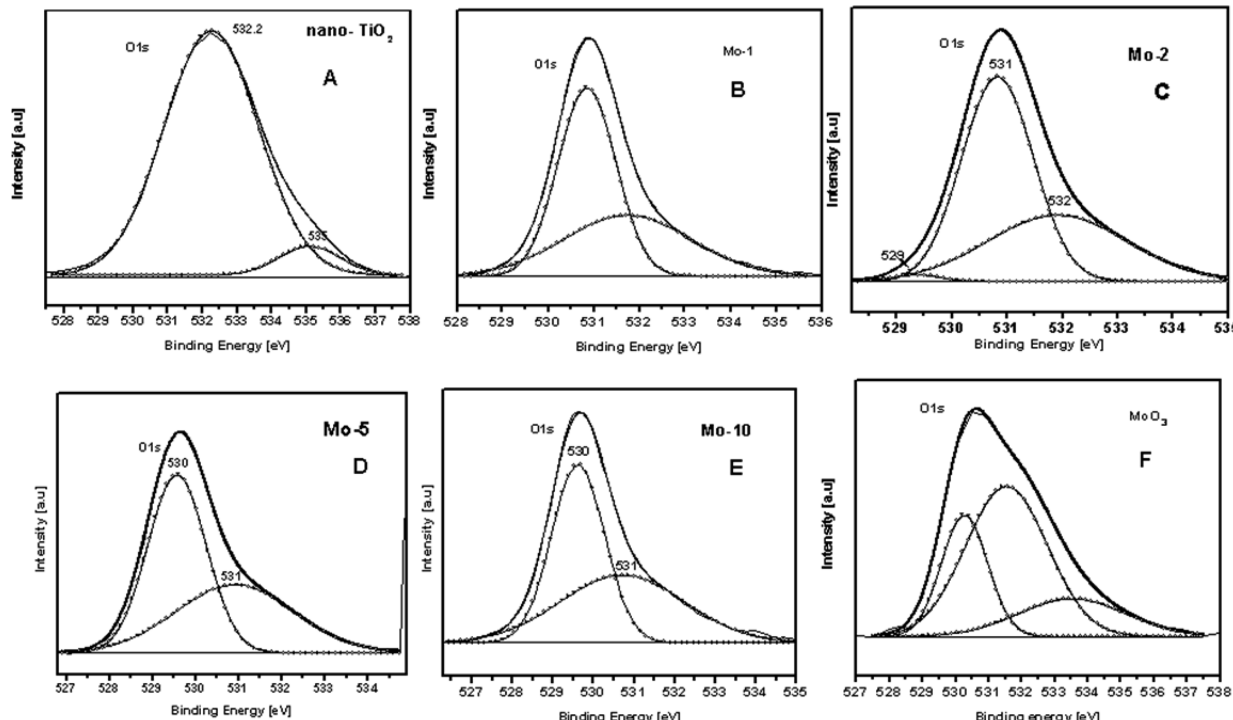


Figure 7. Deconvoluted spectra of O 1s (A) nano TiO₂, (B) Mo-1, (C) Mo-2, (D) Mo-5; (E) Mo-10; and (F) MoO₃.

of Mo in the TiO₂ lattice. This leads us to think that with a higher oxidation state of Mo⁶⁺ being incorporated in the lattice, in order to maintain the charge neutrality of the system, there is formation of nonstoichiometry in the Ti and O sites and disproportionation in the Mo site. The Mo has multiple oxidation states of 5+ and 6+, and the O signal can also be deconvoluted into two peaks. This leads us to the hypothesis that the TiO₂ lattice has certain Ti sites substituted by Mo, while certain Ti sites are vacant. However, Mo itself disproportionates to Mo⁵⁺ and Mo⁶⁺, with some amount of O excess. In addition to this, there is also a definite amount of nano dispersed MoO₃ as a minority phase within the doped TiO₂ anatase lattice. Therefore, we can provide a qualitative insight of Mo doping in the TiO₂ lattice; however, an accurate quantitative estimate of the doping level remains to be made.

e. Electron Microscopy Studies (TEM). Figures 8(A) and 8(B) show the transmission electron micrograph (TEM) of Mo-1 and Mo-5 samples along with the respective selected area electron diffraction (SAED) and EDX pattern. The micrographs suggest that the samples consist of nano particles in the range of 7–10 nm, which are mostly spheroidal in shape. A close examination of the SAED patterns confirms the coexistence of both TiO₂ and the MoO₃ in the Mo-5 sample. The lattice fringes of the system reveal d values representing both the TiO₂ lattice (and Mo-doped TiO₂ lattice) and the MoO₃ lattice. Corroborating our Raman data, the TEM data also provides an evidence of the presence for nano composites of Mo-doped TiO₂ and MoO₃. In the Mo-1 samples, both the SAED pattern and the lattice fringes suggest mostly the presence of anatase TiO₂ rather than the biphasic Mo-TiO₂ and MoO₃. This is obvious as the SAED pattern shows mostly the d values representing the anatase TiO₂. However, the EDX pattern definitely shows the presence of the Mo. Therefore, it strongly suggests the substitutional incorporation of the Mo⁶⁺/Mo⁵⁺ ion in the anatase TiO₂ lattice via doping. This

observation can also be corroborated from the XRD patterns [discussed in X-ray Diffraction Studies (XRD)]. However, from the Mo-2 sample onward, lattice fringes representing two different d values are found, showing the presence of the nano composite phases. The presence of a small amount of the MoO₃ phase along with anatase TiO₂ is quite obvious from the SAED patterns of these samples. The EDS results confirm that in addition to the Mo-doped in the anatase TiO₂ lattice, there must also exist some MoO₃ phase for the stoichiometry to be consistent. Therefore, in corroboration with the Raman results, the TEM also shows the definite presence of the MoO₃ phase along with the Mo-doped TiO₂ anatase sample.

f. Photocatalytic Activity. The photocatalytic activity of these materials was studied under ambient conditions using a photoirradiative source as described earlier in Experimental Section. The absorbance was recorded in the blank experiment at different time intervals for pure Rh-B, excluding any photocatalyst whatsoever. This shows peak maximum at 554 nm along with two smaller peaks at 354 and 260 nm. However, no significant decrement was observed negligible self-degradation of the dye. The adsorption profile of samples was tested by equilibrating the samples with the dye solution in the dark for 30 min followed by recording the UV-visible spectra. There was no decrease in the intensity of the UV-Visible spectra, after adsorption, in any of the samples except for the Mo-2 sample. In the case of the Mo-2 sample, the intensity of the 554 nm peak decreased almost 50% within the first 30 min, indicating the strong adsorption of the dye on the surface of the catalyst. The photoirradiation studies for each catalyst were carried out using the UV source as mentioned in Experimental Section. Differential decrement in intensity of adsorption peak maxima of Rh-B (554 nm) along with time was monitored. However, adsorption of the Rh-B dye over Mo-2 surface shows that the first monolayer of these photocatalysts is not completely covered/saturated by the

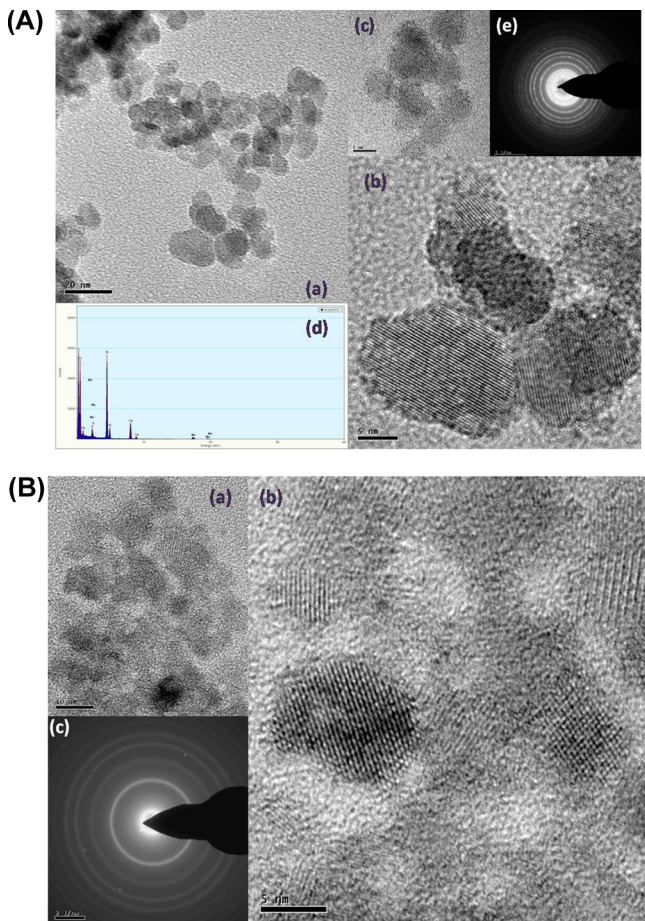


Figure 8. (A) Transmission electron microscopy pattern for the Mo-1 on the scale of (a) 20 nm, (b) 5 nm, (c) 5 nm, (e) SAED pattern for the Mo-1 sample, (d) EDX profile for Mo-1 sample. (B) TEM pattern for the Mo-5 on the scale of (a) 20 nm, (b) 5 nm, and (c) SAED pattern for the Mo-5 sample.

$-\text{OH}$ and H_2O only. A certain amount of dye is also adsorbed directly on the first monolayer of the photocatalytic surface. Therefore, the mechanism of the dye degradation will not be guided by only the free radicals produced in the process of the photoirradiation. The morphological and the electronic transformations owing to the structural changes created by doping or the formation of nano heterostructures will have a direct impact of the photocatalytic efficiency of these materials. This data can be further strengthened by Zeta potential studies (Table 1). An attempt is made to further understand the ways the adsorption may be affected on the surface of these photocatalysts. This is described vividly in the last paragraph of Mechanism.

In the case of pure TiO_2 which is UV active, the complete degradation of dye occurred within 30 min. The intensity of all the peaks (554, 354, and 260 nm) decreases gradually during the photoirradiation and completely disappears after 30 min. New peaks were not observed during the course of the photoirradiation, and all the initial peak intensity were decreased gradually with time. However, the shift in peak intensity was also not observed to any extent, indicating the complete degradation of the dye molecule.

In the case of the Mo-1 sample, complete photodegradation of the Rh-B was demonstrated in 120 min photoirradiated with a UV (source). Any shift in the major peaks was not

observed in this process. In the case of the Mo-2 sample, the complete degradation of the dye is shown in 150 min. However, for the Mo-2 sample, a prior adsorption effect of the dye is discerned. Within 30 min of equilibration of the dye and the catalyst, almost 50% adsorption of the dye on the catalyst surface is observed. Therefore, this extrapolates to an electronic interaction between the dye and the catalytic surface. Similarly, Mo-5 sample also degraded the Rh-B dye completely with a slower kinetics of 180 min to give a clear solution. However, in the case of the Mo-10 sample, the degradation followed further slower kinetics and did not even degrade up to 80% in 240 min. Therefore, the trend with the photodegradation of the Rh-B utilizing a UV source is followed by the given descending trend, as can be seen in Figure 10: $\text{TiO}_2 > \text{Mo-1} > \text{Mo-2} > \text{Mo-5} > \text{Mo-10}$. The above descending trend is in accordance with the presence of the lowering percentage TiO_2 in the Mo- TiO_2 nano heterostructures. The anatase having a band gap of 3.2 eV primarily absorbs in the UV region. The nano anatase TiO_2 structure owing to the quantum confinement effect^{66–68} will further absorb in the UV regime only. The MoO_3 on the other hand has a BG of 2.78 eV, which primarily absorbs in the visible region. The introduction of the Mo in the Mo- TiO_2 system, in effect, provides a continuous lowering of the band gap as a function of Mo-loading in the Mo- TiO_2 -system (as was observed in the DRS studies). Therefore, effectively lower absorption of the UV source will be expected for this series of catalysts with increasing concentration of the Mo. We do observe the same effect with the photocatalysts and, therefore, it can be easily inferred that under the UV irradiative source, it is the TiO_2 band gap absorption that plays a major role.

The photoirradiation of these samples under visible irradiative source, however, deciphers a different account altogether. Figure S.I-1A of the Supporting Information shows the UV-Vis spectra of Rh-B solution differentially irradiated with respect to time with the nano- TiO_2 particles. The intensity of all the peaks (554, 354, and 260 nm) decreases gradually and completely disappears after 240 min. There are no additional peaks in the UV-Vis spectra in the course of the experiment using titania nanoparticles. This suggests that the dye is completely degraded and not only photobleached. In accordance with Watanabe et al.,⁶⁹ the blue shift in the absorption maximum is related to the N-deethylation of Rh-B to Rh, the major intermediate in the degradation of Rh-B. The absence of any hypsochromic shift in dye degradation profile using nano TiO_2 probably disseminates the absence of the N-deethylation channel as a major pathway for complete degradation of the Rh-B dye. MoO_3 has a band gap of 2.78 eV. However, photodegradation of Rh-B dye by MoO_3 (Figure S.I-1B of the Supporting Information) did not complete in 240 min. The Figure S.I-1B of the Supporting Information shows that intensity of the 552 nm peak lowers slowly to 50% within 1 h. Thereafter, the 552 nm peak splits into two peaks, with maxima at 526 and 582 nm, respectively. The photodegradation of the Rh-B does not propagate further. The Rh-B is probably transformed to different organic moiety, which itself is quite stable and therefore has the final ground state. This will be further verified in the mechanistic studies of the dye degradation steps shown later in the manuscript.

The Rh-B photo degradation was then undertaken using a visible irradiated source with the different Mo- TiO_2 samples. Among them the Mo-1 sample took ~240 min to completely degrade the Rh-B dye. Utilizing the visible light irradiation, the Mo-5 sample showed the best (Figure S.I-2 of the Supporting

Information) photocatalytic activity as compared to the undoped TiO_2 and other doped samples, with complete degradation within 120 min, without any shift in peak intensity. In the case of the Mo-10 sample, the photoactivity is sharply lowered. The Mo-10 sample does not completely degrade the Rh-B dye in \sim 240 min. Therefore, with the visible irradiation, the trend for the Mo– TiO_2 (Figure 9) samples signifying the

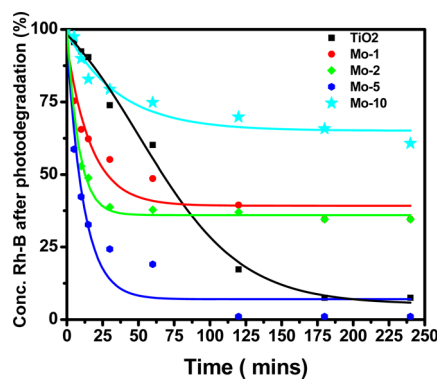


Figure 9. Plot of the time dependent photodegradation of Rh-B using all the photocatalysts under visible irradiation. The Y axis represents the percentage of Rh-B that is left after the photodegradation of the dye by the individual photocatalyst.

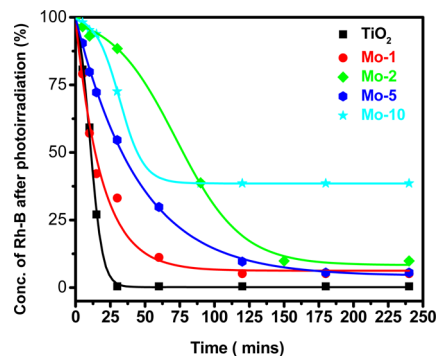


Figure 10. Plot of the time-dependent photodegradation of Rh-B using all the photocatalysts under UV irradiation. The Y axis represents the percentage of Rh-B that is left after the photodegradation of the dye by the individual photocatalyst.

increasing quantity of Mo present is as follows: Mo-1 < Mo-2 < Mo-5 \gg Mo-10. Figure 9 shows the kinetics of the different photocatalysts. It can be stated that under the visible irradiation, as a function of Mo concentration in the Mo– TiO_2 system, photocatalytic activity increases up to Mo-5. However, after Mo-5, the photocatalytic activity of the materials decreases sharply as a function of Mo content in the Mo– TiO_2 system (Figure 9).

The Rh-B is quite adsorbed on the photocatalytic surface and the probable routes for these are enumerated in the later section of the Mechanism in Scheme 4. The TEM, Raman spectra indicates the presence of a separate phase of MoO_3 in the Mo-10 photocatalyst. The Raman data however shows the presence of the nanocomposite phase, starting from Mo-2. Consequently, the XRD data also provides certain evidence of Mo being doped in the TiO_2 anatase lattice. As a function of the Mo percentage in the nanocomposite or the lattice structure, the band gap values are also lowered. However, with the visible irradiative source, photocatalytic activity of

these materials follows the trend as Mo-1 < Mo-2 < Mo-5 \gg Mo-10 (Figure 9). The kinetics of the photodegradation of Rh-B for all the catalysts are fast for the initial few minutes. After that, it becomes quite slow in the rate kinetics. That is reflected in the effect that we get the complete degradation of the dye in longer time, whereas the $t_{1/2}$ is quite low. However, we take the $t_{1/2}$ (represented in Table 1) as the representative time for the kinetic effect of the Rh-B degradation. Therefore, as a function of the Mo content in the system, the photocatalytic activity increases until Mo-5 and then decreases suddenly. The prevalence of the effect due to the change in the band gap due to the Mo-dopant or the MoO_3 – TiO_2 interface conducts a role of importance to a certain degree, as can be seen from Figure 11. However, this is not the only effect as this

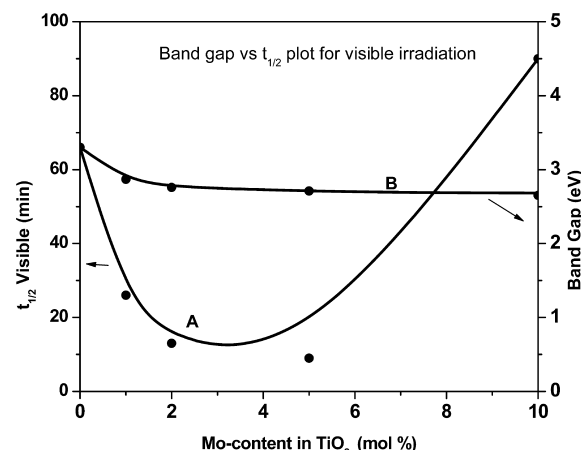


Figure 11. (A) Plot of Mo content in the TiO_2 and the $t_{1/2}$ value (representing the left Y axis). (B) Plot of band gap and the Mo content in the TiO_2 (representing the right Y axis).

could not explain the decline of photoactivity for the Mo-10 sample so sharply from the Mo-5 sample. As we find in Figure 11, the BG and $t_{1/2}$ representing the photocatalytic rate of these samples are comparable. The XPS data definitely show the presence of nonstoichiometry in the Ti sites as a result of the presence of the Mo in the TiO_2 system. However, this nonstoichiometry supposedly created by the cationic deficiencies may also play a role in the promoted photocatalytic activity of these materials with the visible irradiation. Effectively, the Mo also shows a disproportionation to maintain the charge balance in the lattice structure. Perceivably the effect of the nonstoichiometry and the disproportionation could be a result of the Mo being substitutionally doped in the TiO_2 lattice system. This could also result in the change of the resulting oxidation potential of the system, which could play a definite role in augmenting their photocatalytic behavior. However, there emerges a clear picture of the presence of a separate phase of MoO_3 along with the TiO_2 –Mo-doped lattice. The resulting interphase would also play a significant part in the photocatalytic feature of these catalysts. Even the defect sites present in the MoO_3 could be utilized by these catalytic systems. Conceivably the Mo–O will be more covalent in nature as compared to that of the Ti–O bond. In the MoO_3 structure, Mo being in the 6+ state and O being in the 2- state will probably be having more covalency in the Mo–O bond as compared to the TiO_2 or Mo-doped TiO_2 system.^{70–76} The TiO_2 or Mo-doped TiO_2 system should in principle be more ionic in nature. The ionic radius of Mo^{6+} is (0.62 Å), whereas

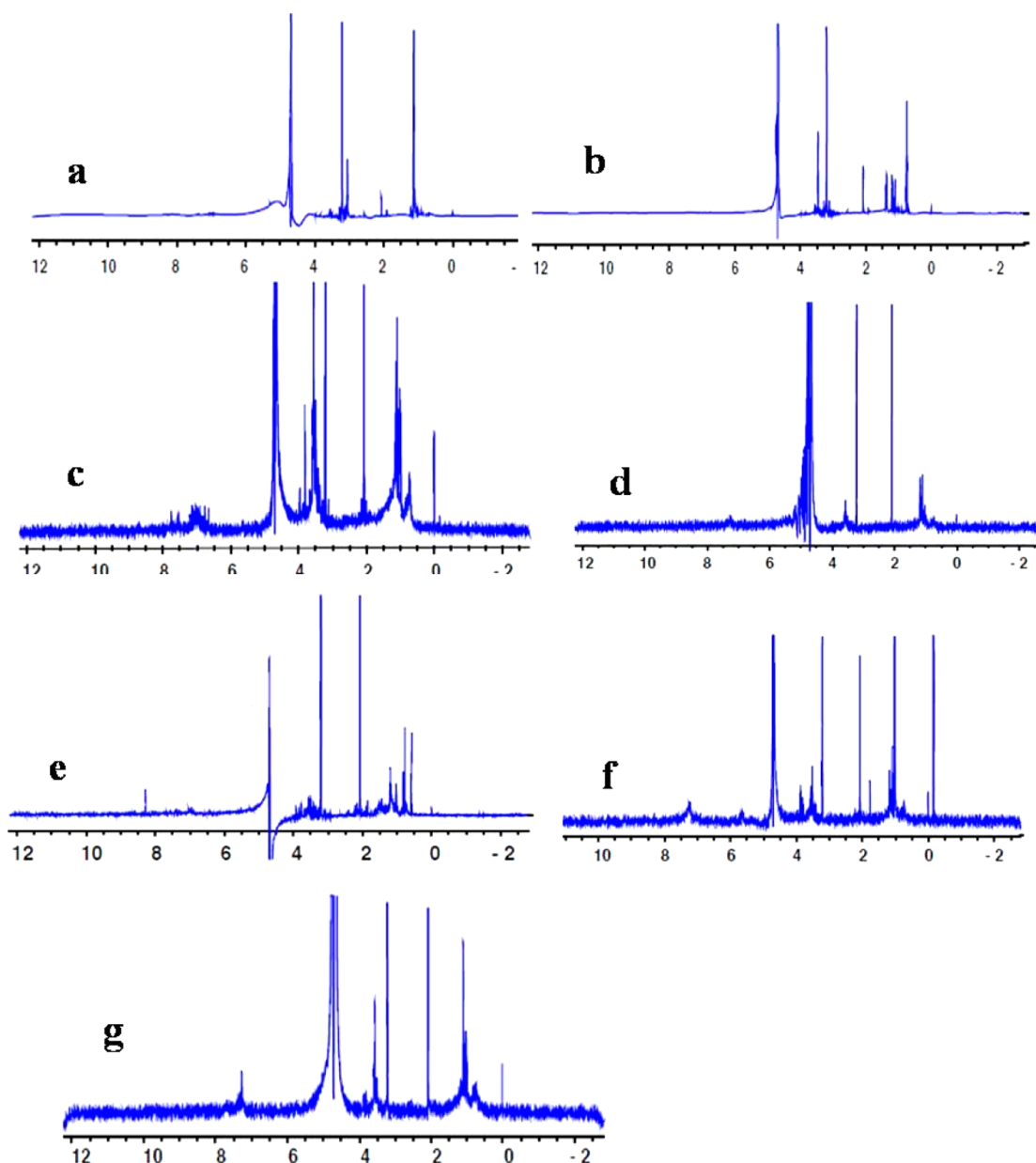


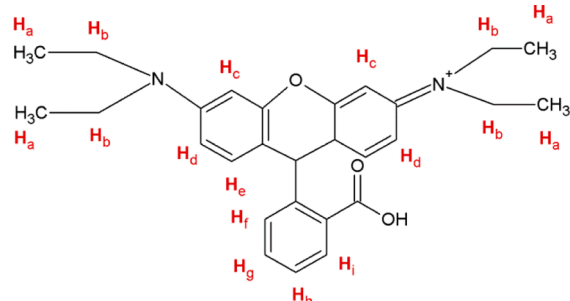
Figure 12. Temporal profile for the proton NMR for (a) Rh–B pure without any photocatalyst or any irradiation. (B) Rh–B which is photodegraded using visible light with the photocatalyst Mo-5 for 0 min after adsorption, (c) 30 min of irradiation, (d) 60 min of irradiation, (e) 120 min of irradiation, (f) Rh–B which is photodegraded using UV irradiation for the Mo-1 photocatalyst for 120 min, (g) Rh–B which is photodegraded using visible light using MoO₃ photocatalyst.

the Ti⁴⁺ is (0.65 Å), which are comparable. With the anion (O²⁻) being the same for both of them, Mo having a stronger charge will be therefore able to polarize the Mo–O bond more than that of the Ti–O bond, leading it to a greater covalent character. [This can be understood in light of the Fajan's Rule].⁷⁷⁻⁷⁹ Therefore, the presence of the MoO₃ separate phase in the nanocomposite system would definitely alter the redox potential of the system along with the change in the band gap of nano composite material. Consequently, this can provide a positive effect for the photocatalytic performance of the nano composite.

g. Mechanism. The proton NMR spectra for the Rh–B dye and the temporal changes observed in the course of the photodegradation of the Rh–B dye are deciphered henceforth. Figure 12 shows the ¹H NMR spectra for pure RhB. Consistent

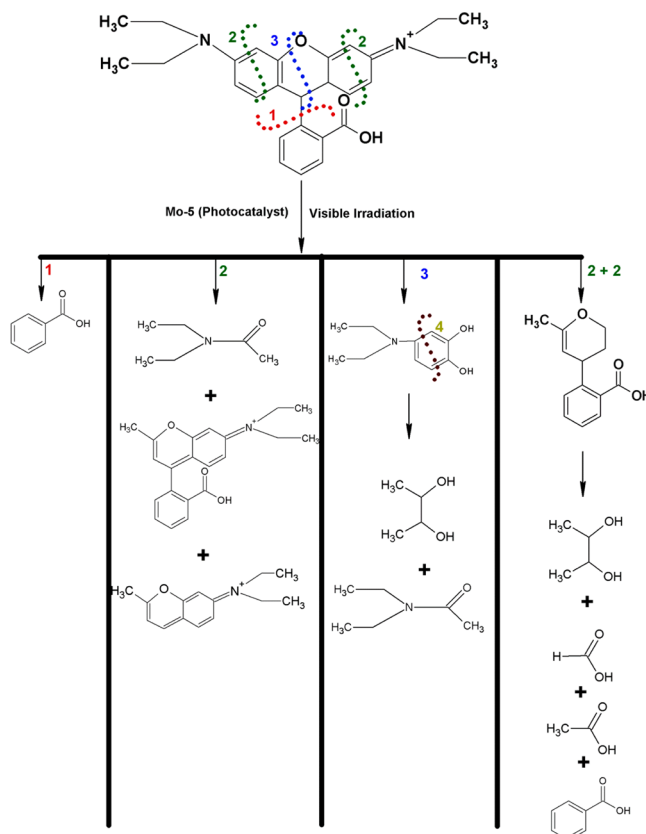
with previous literature,⁸⁰⁻⁸² the NMR signals of the aromatic hydrogen atoms Hc, Hd, He, Hf, Hg, Hh, and Hi [c, d, e, f, g, h, and i are the element H position in the Rh–B structure in (Scheme 2)] are located at 86.53, 6.70–6.73, 6.99–7.02, 7.28–7.30, 7.60–7.65, and 7.90–7.93 ppm, respectively. The Ha represents those of the aliphatic hydrogen in the *N*-diethyl amine group for –CH₃ with chemical shifts present $\sim \delta$ (1.10–1.2) ppm. Equivalently, the Hb represents the methylene group (>CH₂) of *NN*-diethyl amine and is shown in the range of $\sim \delta$ (3.3–3.4) ppm chemical shift.^{80–82}

(i). **Visible Irradiation.** The sequential changes in the proton NMR spectra with time were observed using visible irradiation for Rh–B dye with Mo-5 photocatalyst. The Figure 12 shows the temporal variation in the ¹H NMR spectra after 30 and 120 min of irradiation, respectively. While observing the temporal

Scheme 2. Rhodamine-B with Different Protons**Rhodamine -B**

variation in the ^1H NMR spectra after 120 min several interesting features arise. Initially, we observe a disappearance of several peaks found for the pristine Rh-B without any irradiation. The disappearance of the ^1H NMR peaks are induced at the chemical shift values of δ (6.6–7.8) ppm. This region preferably is dominated by the protons for the aromatic moieties. Their disappearance indicates the absence of the aromatic moieties that were present with the Rh-B structure. Therefore, this may lead to preferable paths through which the photocatalytic cleavage of Rh-B could possibly occur. Simultaneously, there is advent of several new peaks in the ^1H NMR spectra having chemical shift values of δ (0–4.0) ppm. The disappearance of the H_f to H_i (as per Scheme 2 showing the structure of the Rh-B, indicating the different protons present), and the presence of the only one aromatic proton postirradiation shows the possibility of the cleavage path 1 (as shown in Scheme 3) and the formation of the benzoic acid may occur through this path. The formation of the benzoic acid as a visible photodegradation product of Rh-B corroborates with the previous literature, using other spectroscopic tools like Mass/SIMS.^{80–82} However, loss of the H_c and H_d NMR signal after the photocatalytic irradiation study indicates the cleavage route 2 (as per Scheme 3) with the visible irradiation. This may lead to the formation of the amides and subsequent amines and diols. However, there could be a cleavage simultaneously through the route –2 at the same time, as shown in the (2 + 2) [refer to Scheme 3]. This would lead to products of diols and primary acids and benzoic acid along with certain amines. These products can be further cleaved to form smaller molecules like acetic acid and formic acid and further to CO_2 .

The formation of these products as enumerated above is further supplemented by the formation of certain new peaks during the process of the photodegradation of Rh-B. The proton NMR peak at the chemical shift value of δ (0.58) ppm is a sharp high intensity peak, which is generally due to a primary alcohol or acetoyl group.^{80–83} There is small broad peak at δ (0.68) ppm, which suggests formation of $-\text{H}$ of an amide or probably an alkyl $-\text{CH}_3$.^{82–85} The presence of two sharp peaks at δ (0.78) ppm indicates $-\text{H}$ of a $-\text{CH}_3$ group and δ (1–1.2) ppm doublet $-\text{H}$ of a primary alcohol. The new peak at δ (2–2.2) ppm shows the presence of the acetic acid. The secondary amine may be represented by the peak formed at δ (3.15) ppm. There are several peaks between δ (3.2–3.8) ppm, representing different alcohols and phenolic groups. There is a strong peak between δ (3.8–4.0) ppm, suggesting an amide or an ester. The presence of peaks at δ (1–1.2) ppm and δ (3.3–3.4) ppm even after 120 min of photodegradation suggests the complete

Scheme 3. Probable Routes for the Rh-B Photo-Degradation via Visible Irradiation. The Structures are Mere Representatives of the Intermediate Products and Do Not Signify Essentially the Main Final Products

absence of the de-ethylation (a common process seen in the previous literature)^{82,84} pathway for the photodissociation by this photocatalyst.

Figure 12 portrays the photodegradation events after 30 min of photoirradiation. The ensemble of the events is almost the same as that observed in the case of 120 min photoirradiation, with the exception of certain features. After 30 min of the photoirradiation of all the ^1H NMR peaks representing the Rh-B molecule above have lowered down in intensity considerably. However, there was no complete disappearance of any of the above ^1H NMR peaks. Nevertheless several new peaks were found between chemical shifts of δ (0–4) ppm, and a new broad peak was found at $\sim\delta$ (7.5) ppm and the other as described in the previous section of 120 min. This indicates that the time-dependent temporal event of photodissociation of Rh-B is not a singular/stochastic event and follows a kinetic route too. With 30 min of irradiation, the intermediates formed are quite scanty and the Rh-B moiety is still present along with the other intermediate, which is reflected in its UV-vis spectral features of the photodegradation experiments with the visible irradiation.

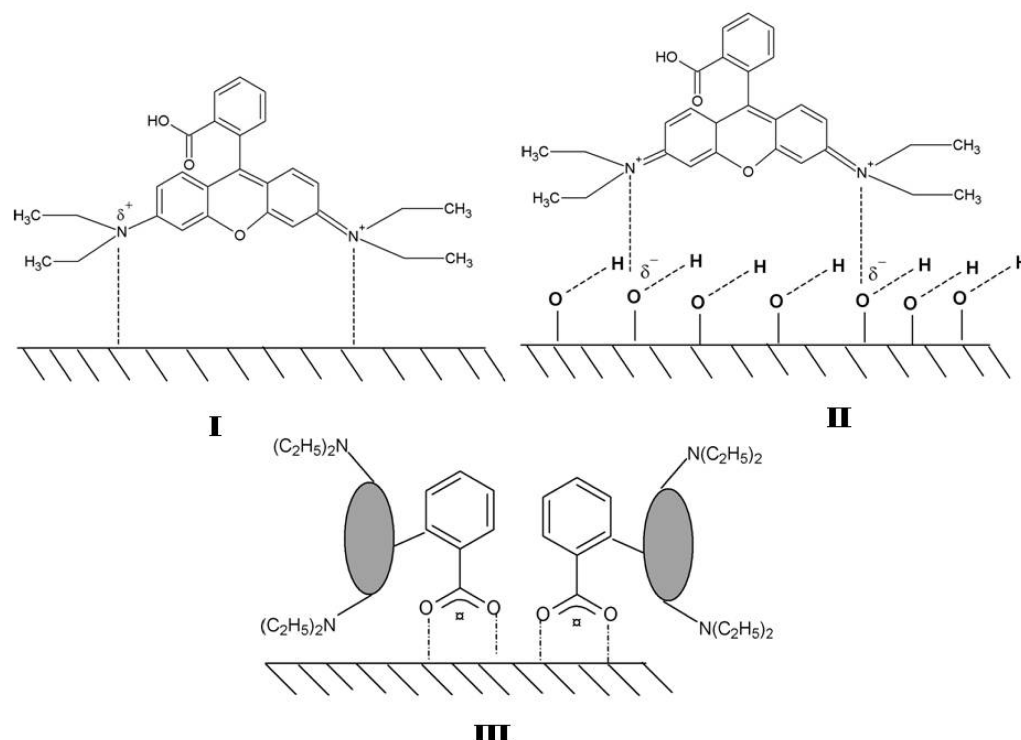
(ii). *UV Irradiation.* The Mo-2 photocatalyst so used is the representative form for the UV irradiation route. The Rh-B dye with the UV irradiation shows lower amounts of intermediate products as formed during the photodegradation process. The intensity of the intermediates as compared to the visible irradiation is lower, and there are fewer peaks observed by the UV irradiation. However, in general talk, the disappearance of the aromatic proton NMR peaks are

comparable with that of the visible analogue, suggesting almost same route of cleavage occurs in the Rh–B moiety with these two irradiations. Occurrence of the new proton NMR peak is again equivalent to that of the visible analogue. Lower intensity of intermediate peaks generally proclaims the faster kinetics for the UV-irradiated process, which is also corroborated from the dye degradation experiments. Therefore, probably Scheme 3 can be considered as a unified route for the cleavage of the Rh–B molecule photocatalytically by these series of photocatalysts.

(iii). *Visible Irradiation with MoO₃*. The ¹H NMR results using MoO₃ itself as a photocatalyst provides us certain further insights about the Rh–B photodegradation by this photocatalyst. The MoO₃ is having a band gap in the region of 2.8 eV. So it makes more sense to check the mechanistic activity of this material under the visible irradiation rather than the UV irradiation. The different temporal features via photo-oxidation of Rh–B shows after even 120 min, there is complete loss of the Hc–Hi peaks as reported previously in the above paragraphs. However, there is a prominent appearance of triplet corresponding to three different aromatic –H in the benzoic acid. This is quite clear in this system and appears in the range of the chemical shift value of δ (6.9–7.05) ppm. Therefore, the cleavage Route 1 (as per Scheme 3) is always happening. This is further supported with the –H of the benzoic acid found at the chemical shift value of δ (8.3) ppm. The lowering/disappearance of the Ha and Hb far lower as compared to the nano composite system of Mo-5. This suggests these species are relatively stable and are present as additionally stable intermediates. Another interesting observation is that the amines and the amides are formed to a very low extent in this system. The absence of the peaks in chemical shift value range of δ (1.6–1.8) ppm and (3.5–4.0) ppm corroborates this data. There is broad peak found for the amines at the chemical shift value of δ (1.4–1.6) ppm with much less intensity. The diols equivalently are also formed to a very less extent, suggesting Route-3 (as represented in Scheme 3) is quite poor in the photo degradation of Rh–B using MoO₃ as the photocatalyst. The acetic acid is present in stronger intensity with chemical shift value referring to δ (3.3) ppm.⁸³ This perhaps indicates that the diols either are formed in lower quantity or are further photo-oxidized to acetic and benzoic acids. However, the absence of the amides could be due to two reasons. The amides can also further oxidize to produce stable acids or are effectively adsorbed on the MoO₃ surface very strongly and are not in the final solution.

The photo-oxidation studied via the UV-vis in the above Photocatalytic Activity indicates clearly that after 120 min, there is formation of a very stable intermediate which does not further photodegrade and is quite stable on the MoO₃ surface. The Zeta potential values show that with the excess amount of Mo in the surface, the negativity of the surface charge is enhanced (Table 1). However, on adsorption of the Rh–B, the negativity is lowered. This phenomenon is observed for the Mo-10 sample also. Therefore, identifying this fact rationally suggests that the amides and the amines will be strongly attracted by MoO₃ surface and owing to the electrostatic attraction between them would stabilize these intermediates further. The presence of the excess amount of MoO₃ (as a separate phase) on the surface rather than the doped Mo will lead to formation of certain stable intermediates. The highly stable intermediates will be strongly detrimental in the photooxidation of Rh–B on these photocatalytic surfaces. Consequently, the presence of the MoO₃ as a nano composite

phase along with the Mo-doped TiO₂ can be detrimental for the Rh–B photodegradation effect as the dye can be adsorbed very strongly on the surface of the MoO₃ as observed for pure MoO₃. However, the most plausible reason for the lowering of the photo activity of the Mo-10 photocatalyst as compared to that of Mo-5 and even TiO₂ may be due to the concurrence of the events as defined above. Equivalently, if we observe the kinetics of the photocatalysts degrading the Rh–B, this also becomes quite apparent. The initial kinetics are quite fast. However, after some time the kinetics slow down quite a bit. This could be correlated between the two effects. The adsorption of certain stable intermediates will happen on almost any MoO₃ surface. This should in turn lower the photoactivity of these photocatalysts. Qualitatively, this could be understood by the fact that the presence of the MoO₃ as different phases with a separate entity from the Mo-doped TiO₂ does change the overall ionicity/covalency of the bonding order for these nanocomposites. As a result, the overall redox-potential of the nanocomposite photocatalyst will also be altered with the differential amount of the separate phase of MoO₃ being present in the nanocomposite. As discussed earlier in the above section, the MoO₃ structure, with Mo being in the 6+ state and O being in the 2– state, will probably be having more covalence in the Mo–O bond as compared to the TiO₂ or Mo-doped TiO₂ system.^{72–78} Therefore, the presence of the MoO₃ separate phase in the nanocomposite system would definitely alter the redox potential of the system, along with the change in the band gap of the nanocomposite material. Consequently, this can provide a positive effect for the photocatalytic performance of the nano-composite. However, as we see the presence, MoO₃ can perceptibly also play an antagonistic role due to the stronger electrostatic attraction between the surface and the amine or the amide-based intermediates. Strong adsorption of the higher electrophilic N-based intermediates over its surface can lead to a very stable intermediate, thereby lowering its photocatalytic activity. The visible irradiation trend for the Mo–TiO₂ samples, signifying the increasing quantity of Mo present is as follows: Mo-1 < Mo-2 < Mo-5 ≫ Mo-10. The Mo-10 being less active than the nano TiO₂. We find that up to Mo-5, the photocatalytic activity increases as a function of Mo content (in the Mo–TiO₂ system). All these photocatalysts are better than the nano TiO₂. However, once we reach Mo-10, there is a sharp decline in the photocatalytic activity as compared to Mo-5 and even nano TiO₂. Another point worth mentioning from the Raman features are that up to Mo-5, the MoO₃ phase is a surface phase, whereas in the Mo-10, there is strong presence of the bulk phase. In the bulk phase, MoO₃ as per the above discussion, according to the mechanistic determination, plays a detrimental role for photoactivity, as certain intermediates get strongly adsorbed on it. The surface MoO₃ along with certain Mo-doping alters the redox potential and positively augments the photocatalytic process. This factor plays a strong role in the Mo-1 to -5 where Mo is doped to an optimum amount, and the MoO₃ is present as a surface phase. However, the second factor where the intermediates get very strongly adsorbed on the MoO₃ surface, which drastically reduces its photocatalytic property, becomes very dominant for the Mo-10 where the MoO₃ is present in the bulk form even. Therefore, there should be an optimum amount of MoO₃ in the nano composite of Mo–TiO₂. Perceivably, this is observed in almost all the present photocatalysts, and as with time, the rate lowers down considerably in almost all of them. However, the point to which

Scheme 4. Probable Structures after Adsorption of Rh-B on the Photocatalytic Surface

its effect becomes detrimental still possess to be an open question and requires further detailed investigation.

The zeta potential values as shown in Table 1 show that almost all of these surfaces are negatively charged. With the surfaces of the catalysts being negative in nature, under all probability the dye will be guided by the electrostatic attraction on being adsorbed on the surface. The Rh-B being a cationic dye, there is a definite possibility of strong electronic interaction for the adsorption effect. Therefore, in all probabilities, the Rh-B can be adsorbed on the surface of the photocatalytic materials via the following routes as given in Scheme 4. Either the nucleophilic N group can be directly adsorbed on the surface via a strong electrostatic interaction as in I or they can be adsorbed over surface $-\text{OH}$ of the photocatalyst. The Rh-B dye degradation is occurring over a solid–liquid interface, and the first monolayer of the photocatalytic surface would be saturated with the hydroxyl groups or the H_2O molecule itself. As found in the photocatalytic data, we seldom find any de-ethylation step for these sets of photocatalyst. The Route III, as shown in Scheme 4, will have initially the de-ethylation step as the major step for the intermediate formation. Therefore, according to us, this would be the least probabilistic step for the adsorption process. Henceforth, the route-II in Scheme 4 could be the most likely route for the adsorption process. The route 1, 2, 3, and 2 + 2 as referred in Scheme 3 may follow subsequently post this adsorption step. The other prospective route of adsorption for the Rh-B dye on the photocatalytic surface could be a π -anionic interaction between them.⁸⁰ The surface (negatively charged therefore conceivably anionic in nature) and the delocalized π -electrons of the Rh-B. Generally the π -anionic interaction possesses energetically quite low values.⁸³ Consequently, if the system possesses heteroatoms, the π -anionic interaction will show further lower energy values.⁸⁶ This would therefore least

perturb a hydrated surface as in that of the present scenario. Therefore, this route of adsorption could be neglected.

Therefore, overall the mechanistic studies by the ex situ NMR hints to the facts that UV and visible irradiation do not have different routes for the photo-oxidation process by these photocatalysts. This could suggest that the electron and the hole produced by them in this process with the differential UV or the visible-irradiated sources do by some means having equiergic electrons and the holes resulting in similar intermediate routes. However, the process of the equiergic production of this e^-/h^+ pair by the differential source is still an open question to be addressed. It could also be a result of the intermediate surface, resulting in the typically equivalent defect sites.

4. CONCLUSION

The photodegradation study of the Rh-B dye was performed utilizing a TiO_2 -based photocatalyst, which shows the effects of both the Mo-doping and incorporation of nano dispersed MoO_3 . The primary characterization techniques do confirm such a structure. XRD shows the formation of the MoO_3 starting from the Mo-5 sample. The Raman spectroscopic data along with TEM studies, however, show the signature of MoO_3 in all samples (Mo-1 to Mo-10). This is not surprising, since these spectroscopic techniques are more sensitive to the presence of minority phases. The DRS studies indicate that the samples are indirect band gap semiconductors. The calculated band gap, from the Kubelka–Munk plots, range from (3.24 to 2.65) eV, decreasing as a function of the Mo content. The XPS study appears to indicate the presence of cationic deficient sites in the TiO_2 anatase lattice along with a disproportionation in the oxidation state of Mo. There is also positive evidence for the presence of excess oxygen in the nano composite lattice. The XPS also positively shows the Mo-doping in the TiO_2 lattice. The UV-excited photocatalytic degradation of Rh-B is

primarily dictated by the quantitative presence of anatase TiO_2 in the Mo– TiO_2 system. However, the photocatalytic degradation of Rh–B, with the visible light is clearly correlated with the Mo content, increasing from Mo-1 to Mo-5. However, there is a sharp decrease in the photoactivity from Mo-5 to Mo-10, the latter being even less active than undoped TiO_2 . Thus, the trend in the activity of these photocatalysts can be summarized as Mo-1 < Mo-2 < Mo-5 ≫ Mo10 for irradiation with visible light. This trend in the photocatalytic activity of these materials can be qualitatively understood in terms of structure–activity correlation. The presence of the nano dispersed MoO_3 phase in the nanocomposite system would definitely alter the redox potential of the system as well as the band gap of nanocomposite material and thereby affect the photocatalytic performance. Similarly, the $\text{Mo}^{6+}/\text{Mo}^{5+}$ dopants could also affect the redox potential of the nano composite and augment the photo-oxidation process. The MoO_3 phase in samples Mo-1 to Mo-5 is probably present as a surface phase, which clearly augments the photoactivity of these materials by altering its redox potential. However, in Mo-10, the excess amount of MoO_3 is present as the bulk phase rather than the surface phase and doped Mo. This will lead to formation of certain very stable intermediates, which will be strongly detrimental to the photo-oxidation of Rh–B, thereby drastically lowering the photoactivity of Mo-10 as compared to the other Mo-5, etc. Ex situ NMR studies shows different intermediates and different probable routes of the Rh–B dye degradation. The stable intermediates were formed by a direct oxidative fragmentation route, without any evidence for the de-ethylolation route. The intermediates obtained were benzoic acid, different amines, diols, and acids (mostly pertaining to formic and acetic acid). We are also quite positive about the adsorption of the Rh–B dye on the catalytic surface via the N-charge centers of the Rh–B. The photo-oxidation can be expected to lead to the complete mineralization of the Rh–B to give CO_2 .

ASSOCIATED CONTENT

Supporting Information

Ten images representing temporal profile for the UV–vis spectra of Rh–B dye using (A) TiO_2 (nano) photocatalyst, (B) MoO_3 photocatalyst, temporal profile for the UV–vis spectra of Rh–B dye using Mo-5 photocatalyst, effect of H_2O_2 in the rate of reaction, dye + Mo-10 sample irradiated under visible irradiation, dye + Mo-5 sample irradiated under UV irradiation, effect of pH in the rate of reaction, effect of the O_2 flow in the rate of reaction, effect of the –OH group flow in the rate of reaction, cyclovoltogram of Rh–B and Rh–B after photo-irradiation for 1 h with the Mo-5, plot of the UV–vis spectrum for the rhodamine-B dye under visible irradiation without any catalyst (blank data). This material is available free of charge via the Internet at <http://pubs.acs.org>.

AUTHOR INFORMATION

Corresponding Author

*E-mail: kaustava@barc.gov.in. Tel: +0091-22-25590271. Fax: 0091-22-2550 5151; 0091-22-2551 9613.

Present Address

^{II}Department of Physics, Dr. Hari Singh Gour University, Sagar, MP, 470003, India.

Notes

The authors declare no competing financial interest.

ACKNOWLEDGMENTS

We thank Dr. Chiranjib Majumder, ChD, BARC, for fruitful discussions and Mr. V.S. Tripathi of RPCD, BARC, for helping us in taking the CV of the dyes.

REFERENCES

- O'Regan, B.; Grätzel, M. A Low-Cost, High-Efficiency Solar Cell Based on Dye-Sensitized Colloidal TiO_2 Films. *Nature* **1991**, *353*, 737–740.
- Kitano, M.; Matsuoka, M.; Ueshima, M.; Anpo, M. Recent Developments in Titanium Oxide-Based Photocatalysts. *Appl. Catal., A* **2007**, *325*, 1–14.
- Hoffmann, M. R.; Martin, S. T.; Choi, W.; Bahnemann, D. W. Environmental Applications of Semiconductor Photocatalysis. *Chem. Rev.* **1995**, *95*, 69–96.
- Linsebigler, A. L.; Lu, G.; Yates, J. T. Photocatalysis on TiO_2 Surfaces: Principles, Mechanisms, and Selected Results. *Chem. Rev.* **1995**, *95*, 735–758.
- Fujishima, A.; Rao, T. N.; Tryk, D. A. Titanium Dioxide Photocatalysis. *J. Photochem. Photobiol., C* **2000**, *1*, 1–21.
- Carp, O.; Huisman, C. L.; Reller, A. Photoinduced Reactivity of Titanium Dioxide. *Prog. Solid State Chem.* **2004**, *32*, 33–177.
- Fujishima, A.; Zhang, X.; D, A. Tryk, TiO₂ Photocatalysis and Related Surface Phenomena. *Surf. Sci. Rep.* **2008**, *63*, 515–582.
- Bregani, F.; Casale, C.; Depero, L. E.; Natali-Sora, I.; Robba, D.; Sangaletti, L.; Toledo, G. P. Temperature Effects on the Size of Anatase Crystallites in Mo– TiO_2 and W– TiO_2 Powders. *Sens. Actuators, B* **2004**, *31*, 25–28.
- Kubacka, A.; Colón, G.; Fernández-García, M. Cationic (V, Mo, Nb, W) Doping of TiO_2 -Anatase: A Real Alternative for Visible Light-driven Photocatalysts. *Catal. Today* **2009**, *143*, 286–292.
- Silva, N. U.; Nunes, T. G.; Saraiva, M. S.; Shalamzari, M. S.; Vaz, P. D.; Monteiro, O. C.; Nunes, C. D. Photocatalytic Degradation of Rhodamine B using Mo Heterogeneous Catalysts Under Aerobic Conditions. *Appl. Catal., B* **2012**, *113–114*, 180–191.
- Li, Y. X.; Chen, J.; Wang, L. Effect of Doping Mode on the Photocatalytic Activities of Mo/TiO₂. *J. Photochem. Photobiol., A* **2004**, *163*, 517–522.
- Tan, K.; Zhang, H.; Xie, C.; Zheng, H.; Gu, Y.; Zhang, W. F. Visible-Light Absorption and Photocatalytic Activity in Molybdenum- and Nitrogen-Co Doped TiO_2 . *Catal. Commun.* **2000**, *11*, 331–333.
- Štengl, V.; Bakardjieva, S. Molybdenum-Doped Anatase and its Extraordinary Photocatalytic Activity in the Degradation of Orange II in the UV and Vis Regions. *J. Phys. Chem. C* **2010**, *114*, 19308–19317.
- Gomathi Devi, L.; Narasimha Murthy, B. Characterization of Mo Doped TiO_2 and its Enhanced Photo, Catalytic Activity Under Visible Light. *Catal. Lett.* **2008**, *125*, 320–330.
- Gomathi Devi, L.; Narasimha Murthy, B.; Kumar, S. G. Heterogeneous Photo Catalytic Degradation of Anionic and Cationic Dyes Over TiO_2 and TiO_2 Doped with Mo^{6+} Ions Under Solar Light: Correlation of Dye Structure and its Adsorptive Tendency on the Degradation Rate. *Chemosphere* **2009**, *76*, 1163–1166.
- Gomathi Devi, L.; Kumar, S. G.; Narasimha Murthy, B.; Kottam, N. Influence of Mn^{2+} and Mo^{6+} Dopants on the Phase Transformations of TiO_2 Lattice and its Photo Catalytic Activity Under Solar Illumination. *Catal. Commun.* **2009**, *10*, 794–798.
- Song, K. Y.; Park, M. K.; Kwon, Y. T.; Lee, H. W.; Chung, W. J.; Lee, W. I. Preparation of Transparent Particulate $\text{MoO}_3/\text{TiO}_2$ and WO_3/TiO_2 Films and their Photocatalytic Properties. *Chem. Mater.* **2001**, *13*, 2349–2355.
- Vinod, K. N.; Puttaswamy, T. K.; Gowda, N. N. Oxidative Decolorization of Triphenylmethane Dyes by Chloramine-T in Alkaline Medium Catalyzed by Pd(II): A Comparative Spectrophotometric Kinetic and Mechanistic Approach. *J. Mol. Catal. A: Chem.* **2009**, *298*, 60–68.
- Ayed, L.; Chaieb, K.; Cheref, A.; Bakhrouf, A. Biodegradation of Triphenylmethane Dye Malachite Green by *Sphingomonas paucimobilis*. *World J. Microbiol. Biotechnol.* **2009**, *25*, 705–711.

- (20) Chen, C.; Lu, C. S. Mechanistic Studies of the Photocatalytic Degradation of Methyl Green: An Investigation of Products of the Decomposition Processes. *Environ. Sci. Technol.* **2007**, *41*, 4389–4396.
- (21) Wu, T.; Liu, G.; Zhao, J.; Hidaka, H.; Serpone, N. Photoassisted Degradation of Dye Pollutants. V. Self-Photosensitized Oxidative Transformation of Rhodamine B under Visible Light Irradiation in Aqueous TiO₂ Dispersions. *J. Phys. Chem. B* **1998**, *102*, 5845–5851.
- (22) Park, H.; Choi, W. Photocatalytic Reactivities of Nafion-Coated TiO₂ for the Degradation of Charged Organic Compounds under UV or Visible Light. *J. Phys. Chem. B* **2005**, *109*, 11667–11674.
- (23) Bhattacharyya, K.; Varma, S.; Tripathi, A. K.; Bharadwaj, S. R.; Tyagi, A. K. Effect of Vanadia Doping and its Oxidation State on the Photocatalytic Activity of TiO₂ for Gas-Phase Oxidation of Ethene. *J. Phys. Chem. C* **2008**, *112*, 19102–19112.
- (24) Hwang, T. L.; Shaka, A. J. Water Suppression That Works. Excitation Sculpting Using Arbitrary Wave-Forms and Pulsed-Field Gradients. *J. Magn. Reson., Ser. A* **1995**, *112*, 275–279.
- (25) Seguin, L.; Figlarz, M.; Cavagnat, I. R.; Lasskques, J. C. Infrared and Raman Spectra of MoO₃ Molybdenum trioxides and MoO₃·xH₂O Molybdenum Trioxide Hydrates. *Spectrochim. Acta, Part A* **1995**, *51*, 1323–1344.
- (26) Banwell, N.; McCash, E. M. *Fundamentals of Molecular Spectroscopy*, 4th ed.; McGraw-Hill Publishing: New York, 1994.
- (27) Ohsaka, T.; Izumi, F.; Fujiki, Y. Raman Spectrum of Anatase TiO₂. *J. Raman Spectrosc.* **1978**, *7*, 321–324.
- (28) Zhang, Y. H.; Chan, C. K.; Porter, J. F.; Guo, W. Micro-Raman Spectroscopic Characterization of Nanosized TiO₂ Powders Prepared by Vapor Hydrolysis. *J. Mater. Res.* **1998**, *13*, 2602–2609.
- (29) Busca, G.; Ramis, G.; Amores, J. M. G.; Escribano, V. S.; Piaggio, P. FT Raman and FT-IR Studies of Titania's and Metatitanate Powders. *J. Chem. Soc., Faraday Trans.* **1994**, *90*, 3181–3190.
- (30) Kelly, S.; Pollak, F. H.; Tomkiewicz, M. Raman Spectroscopy as a Morphological Probe for TiO₂ Aerogels. *J. Phys. Chem. B* **1997**, *101*, 2730–2734.
- (31) Eryigit, R.; Herman, I. P. Lattice Properties of Strained GaAs, Si, and Ge Using A Modified Bond-Charge Model. *Phys. Rev. B* **1996**, *53*, 7775–7784.
- (32) Kubacka, A.; Fernández-García, M.; Colónb, G. Nanostructured Ti-M Mixed-Metal Oxides: Toward a Visible Light-Driven Photocatalyst. *J. Catal.* **2008**, *254*, 272–284.
- (33) Hsien, Y. H.; Chang, C. F.; Chen, Y. H.; Cheng, S. Photodegradation of Aromatic Pollutants in Water over TiO₂ Supported on Molecular Sieves. *Appl. Catal., B* **2001**, *31*, 241–249.
- (34) Tuel, L.; Hubert-Pfalzgraf, G. Nanometric Monodispersed Titanium Oxide Particles on Mesoporous Silica: Synthesis, Characterization, and Catalytic Activity in Oxidation Reactions in the Liquid Phase. *J. Catal.* **2003**, *217*, 343–353.
- (35) Gao, X.; Wachs, I. E. Titania–Silica as Catalysts: Molecular Structural Characteristics and Physico-Chemical Properties. *Catal. Today* **1999**, *51*, 233–254.
- (36) Tubbs, M. R. MoO₃ layers: Optical Properties, Colour Centres, and Holographic Recording. *Phys. Status Solidi A* **1974**, *21*, 253–260.
- (37) Deb, S. K.; Chopoorian, J. A. Optical Properties and Color-Center Formation in Thin Films of Molybdenum Trioxide. *J. Appl. Phys.* **1966**, *37*, 4818–4825.
- (38) Schirmer, O. F.; Wittwer, V.; Baur, G.; Brandt, G. Dependence of WO₃ Electrochromic Absorption on Crystallinity. *J. Electrochem. Soc.* **1977**, *124*, 749–753.
- (39) Kubelka, P.; Munk-Aussig, F. Ein Beitrag zur Optik der Farbanstriche. *Zeitschrift für Technische Physik* **1931**, *12*, 593–601.
- (40) Elder, S. H.; Cot, F. M.; Su, Y.; Heald, S. M.; Tyryshkin, A. M.; Bowman, M. K.; Gao, Y.; Joly, A. G.; Balmer, M. L.; Kolwaite, C. A.; et al. The Discovery and Study of Nanocrystalline TiO₂-(MoO₃) Core–Shell Materials. *J. Am. Chem. Soc.* **2000**, *122*, 5138–5146.
- (41) Rozzi, A.; Manghi, F.; Parmigiani, F. *Ab Initio* Fermi Surface and Conduction-Band Calculations in Oxygen-Reduced MoO₃. *Phys. Rev. B* **2003**, *68* (075106), 1–6.
- (42) Qiang, C.; Hong-Hong, C. Ab Initio Calculations of Electronic Structure of Anatase TiO₂. *Chin. Phys. (Beijing, China)* **2004**, *13*, 2121–2125.
- (43) Jeziorowski, H.; Knözinger, H. Raman and Ultraviolet Spectroscopic Characterization of Molybdena on Alumina Catalysts. *J. Phys. Chem.* **1979**, *83*, 1166–1173.
- (44) Zingg, S.; Makovsky, L. E.; Tischer, R. E.; Brown, F. R.; Hercules, D. M. A Surface Spectroscopic Study of Molybdenum-Alumina Catalysts Using X-ray Photoelectron, Ion-scattering, and Raman Spectroscopies. *J. Phys. Chem.* **1980**, *84*, 2898–2906.
- (45) Chan, S. S.; Iwachs, I. E.; Murrell, L. L.; Wang, L.; Hall, W. K. In situ Laser Raman Spectroscopy of Supported Metal Oxides. *J. Phys. Chem.* **1984**, *88*, 5831–5835.
- (46) Ruiz, P. M.; Delmon, B.; Knözinger, H. Oxygen-Exchange Properties of MoO₃: An *in situ* Raman Spectroscopy Study. *J. Phys. Chem.* **1994**, *98*, 11269–11275.
- (47) Del Arco, M.; Carrazán, S. R. G.; Martín, C.; Rives, V.; García-Ramos, J. V.; Carmona, P. A Laser Raman Spectroscopy Study of Molybdenum Oxide Supported On Alumina and Titania. *Spectrochim. Acta* **1994**, *50*, 2215–2221.
- (48) Kakuta, N.; Tohji, K.; Udagawa, Y. Molybdenum Oxide Structure on Silica-Supported Catalysts Studied by Raman Spectroscopy and EXAFS. *J. Phys. Chem.* **1988**, *92*, 2583–2587.
- (49) Desikan, N.; Huang, L.; Oyama, S. T. Oxygen Chemisorption and Laser Raman Spectroscopy of Unsupported and Silica-Supported Molybdenum Oxide. *J. Phys. Chem.* **1991**, *95*, 10050–10056.
- (50) Desikan, N.; Huang, L.; Oyama, S. T. Structure and Dispersion of Molybdenum Oxide Supported on Alumina and Titania. *J. Chem. Soc., Faraday Trans.* **1992**, *88*, 3357–3365.
- (51) Huckel, W. *Structural Chemistry of Inorganic Compounds*; Elsevier Publishing: New York, 1951; Vol. 2, pp 678–685.
- (52) Andersson, G.; Magneli, A. On the Crystal Structure of Molybdenum Trioxide. *Acta Chem. Scand.* **1950**, *4*, 793–797.
- (53) Kubacka, A.; Fernandez Garcia, M.; Colónb, G. Advanced Nano Architectures for Solar Photocatalytic Applications. *Chem. Rev.* **2012**, *112*, 1555–1614.
- (54) Kumar, P. M.; Badrinarayanan, S.; Sastry, M. Nanocrystalline TiO₂ Studied by Optical, FT-IR and X-Ray Photoelectron Spectroscopy: Correlation to Presence of Surface. *Thin Solid Films* **2000**, *358*, 122–130.
- (55) Zhang, S.; Ogale, S. B.; Yu, W.; Gao, X.; Liu, T.; Ghosh, S.; Das, G. P.; Wee, A. T. S.; Greene, R. L.; Venkatesan, T. Electronic Manifestation of Cation-Vacancy-Induced Magnetic Moments in a Transparent Oxide Semiconductor: Anatase Nb:TiO₂. *Adv. Mater.* **2009**, *21*, 2282–228.
- (56) Gutierrez, A.; Johansson, B. T. Theoretical Structure Determination of γ -Al₂O₃. *Phys. Rev. B* **2001**, *65* (012101), 1–4.
- (57) Bertrand, P. A. XPS Study of Chemically Etched GaAs and InP. *J. Vac. Sci. Technol.* **1981**, *18*, 28–33.
- (58) Moulder, J. F.; Stickle, W. F.; Sobol, P. E.; Bomben, K. D. *Handbook of X-Ray Photoelectron Spectroscopy*; Physical Electronics, Inc.: Chanhassen, MN, 1995.
- (59) Oswald, S.; Brückner, W. XPS Depth Profile Analysis of Non-Stoichiometric NiO Films. *Surf. Interface Anal.* **2004**, *36*, 17–22.
- (60) Tabata, K.; Hirano, Y.; Suzuki, E. XPS Studies on the Oxygen Species of LaMn_{1-x}Cu_xO_{3+x}. *Appl. Catal., A* **1998**, *170*, 245–254.
- (61) Kosova, N. V.; Kaichev, V. V.; Bukhtiyarov, V. I.; Kellerman, D. G.; Devyatkina, E. T.; Larina, T. V. Electronic State of Cobalt and Oxygen Ions in Stoichiometric and Non Stoichiometric Li_{1+x}CoO₂ before and after Delithiation According to XPS and DRS. *J. Power Sources* **2003**, *119*–121, 669–673.
- (62) Merino, N. A.; Barbero, B. P.; Eloy, P.; Cadus, L. E. La_{1-x}Ca_xCoO₃ Perovskite-Type Oxides: Identification of the Surface Oxygen Species by XPS. *Appl. Surf. Sci.* **2006**, *253*, 1489–1493.
- (63) Kollbek, K.; Sikora, M.; Kapusta, C.; Szlachetko, J.; Zakrzewska, K.; Kowalski, K.; Radecka, M. X-Ray Spectroscopic Methods in the Studies of Nonstoichiometric TiO_{2-x} Thin Films. *Appl. Surf. Sci.* **2013**, *281*, 100–104.

- (64) Alyoshin, V. A.; Romanova, I. P.; Mikhailova, D.; Oswald, S.; Senyshyn, A.; Ehrenberg, H. Oxygen Nonstoichiometry of Tetragonal $\text{La}_{2-x}\text{Sr}_x\text{CuO}_{4-\delta}$ ($x = 0.15\text{--}1.2$) and in Situ XPS Studies at Elevated Temperatures. *J. Phys. Chem. A* **2010**, *114*, 13362–13369.
- (65) Vovk, G.; Chen, X.; Mims, C. A. In Situ XPS Studies of Perovskite Oxide Surfaces under Electrochemical Polarization. *J. Phys. Chem. B* **2005**, *109*, 2445–245.
- (66) Hsien, Y. H.; Chang, C. F.; Chen, Y. H.; Cheng, S. Photodegradation of Aromatic Pollutants in Water over TiO_2 Supported on Molecular Sieves. *Appl. Catal., B* **2001**, *31*, 241–249.
- (67) Tuel, L.; Hubert-Pfalzgraf, G. Nanometric Monodispersed Titanium Oxide Particles on Mesoporous Silica: Synthesis, Characterization, and Catalytic Activity in Oxidation Reactions in the Liquid Phase. *J. Catal.* **2003**, *217*, 343–353.
- (68) Gao, X.; Wachs, I. E. Titania–Silica as Catalysts: Molecular Structural Characteristics and Physico-Chemical Properties. *Catal. Today* **1999**, *51*, 233–254.
- (69) Watanabe, T.; Takizawa, T.; Honda, K. Photocatalysis Through Excitation of Adsorbates. 1. Highly Efficient N-Deethylation of Rhodamine B Adsorbed to Cadmium Sulfide. *J. Phys. Chem.* **1977**, *81*, 1845–1851.
- (70) Reddy, B. M.; Chowdhury, B.; Smirniotis, P. G. An XPS Study of the Dispersion of MoO_3 on $\text{TiO}_2\text{--ZrO}_2$, $\text{TiO}_2\text{--SiO}_2$, $\text{TiO}_2\text{--Al}_2\text{O}_3$, $\text{SiO}_2\text{--ZrO}_2$, and $\text{SiO}_2\text{--TiO}_2\text{--ZrO}_2$ Mixed Oxides. *Appl. Catal., A* **2001**, *211*, 19–30.
- (71) Albaret, T.; Finocchi, F.; Noguera, C. First Principles Simulations of Titanium Oxide Clusters and Surfaces. *Faraday Discuss.* **2000**, *114*, 285–304.
- (72) Rodriguez, J. A.; Maiti, A. Adsorption and Decomposition of H_2S on MgO (100), NiMgO (100), and ZnO (0001) Surfaces: A First-Principles Density Functional Study. *J. Phys. Chem. B* **2000**, *104*, 3630–3638.
- (73) Potrzebowski, M. J.; Blaszczyk, J.; Wieczorek, M. W.; Klinowski, J. Solid-State NMR and X-ray Diffraction Studies of the Geometry and Intramolecular Dynamics of Bis (organothiophosphoryl) Dichalcogenides. *J. Chem. Phys.* **1999**, *101*, 8077–8087.
- (74) Bredow, T.; Apra, E.; Catti, M.; Pacchioni, G. Cluster and Periodic *Ab-Initio* Calculations on K/TiO_2 (110). *Surf. Sci.* **1998**, *418*, 150–165.
- (75) Casarin, M.; Maccato, C.; Vittadini, A. An LCAO-LDF Study of the Chemisorption of H_2O and H_2S on $\text{ZnO}(0001)$ and $\text{ZnO}(10\bar{1}0)$. *Surf. Sci.* **1997**, *377*–379, 587–591.
- (76) Scamehorn, C. A.; Harrison, N. M.; McCarthy, M. I. Observation of the Second Ordered Phase of Water on the $\text{MgO}(100)$ surface: Low Energy Electron Diffraction and Helium Atom Scattering Studies. *J. Chem. Phys.* **1994**, *101*, 1547–1554.
- (77) Fajans, K. Struktur und Deformation der Elektronenfüllen in ihrer Bedeutung für die chemischen und optischen Eigenschaften anorganischer Verbindungen. *Naturwissenschaften* **1923**, *11*, 165–172.
- (78) Fajans, K.; Joos, G. Molrefraktion von Ionen und Molekülen im Lichte der Atomstruktur. *Zeitschrift für Physik* **1924**, *23*, 1–46.
- (79) Fajans, K. Die Eigenschaften salzartiger Verbindungen und Atombau. *Z. Kristallogr.* **1925**, *61*, 18–48.
- (80) Li, J.; Ma, W.; Lei, P.; Zhao, J. Detection of Intermediates in the TiO_2 -Assisted Photodegradation of Rhodamine B under Visible Light Irradiation. *J. Environ. Sci.* **2007**, *19*, 892–896.
- (81) Liu, G.; Zhao, J. Photocatalytic Degradation of Dye Sulforhodamine B: A Comparative Study of Photocatalysis with Photosensitization. *New J. Chem.* **2000**, *24*, 411–417.
- (82) Wu, T.; Liu, G.; Zhao, J.; Hidaka, H.; Serpone, N. Photoassisted Degradation of Dye Pollutants. V. Self-Photosensitized Oxidative Transformation of Rhodamine B under Visible Light Irradiation in Aqueous TiO_2 Dispersions. *J. Phys. Chem. B* **1998**, *102*, 5845–5851.
- (83) Yu, S.; Yang, H.; He, C.; Sun, C.; Ju, Y. Visible Light-Driven Photocatalytic Degradation of Rhodamine B over NaBiO_3 : Pathways and Mechanism. *J. Phys. Chem. A* **2009**, *113*, 10024–10032.
- (84) Silverstein, R. M.; Webster, F. X. *Spectrometric Identification of Organic Compounds*, Wiley Student Edition, 6th ed.; 2005; pp 144–216.
- (85) Fu, H.; Pan, C.; Yao, W.; Zhu, Y. Visible-Light-Induced Degradation of Rhodamine B by Nanosized Bi_2WO_6 . *J. Phys. Chem. B* **2005**, *109*, 22432–22439.
- (86) Dawson, R. E.; Hennig, A.; Weimann, D. P.; Emery, D.; Ravikumar, V.; Montenegro, J.; Takeuchi, T.; Gabutti, S.; Mayor, M.; Mareda, J.; et al. Experimental Evidence For The Functional Relevance Of Anion– π Interactions. *Nat. Chem.* **2010**, *2*, 533–538.